Westfälische
Wilhelms-Universität
Münster

Characterization of the Münster Dual Phase Xenon TPC and of a Newly Developed Magnetically Driven Piston Pump

Master Thesis

Axel Buß

Westfälische Wilhelms-Universität Münster
Institut für Kernphysik
AG Prof. Dr. C. Weinheimer

Themensteller: Prof. Dr. C. Weinheimer
Zweitgutachter: Prof. Dr. J. Wessels

Münster, April, 11th 2016

Plagiatserklärung der / des Studierenden

Hiermit versichere ich, dass die vorliegende Arbeit über "Characterization of the Münster Dual Phase Xenon TPC and of a Newly Developed Magnetically Driven Piston Pump selbstständig verfasst worden ist, dass keine anderen Quellen und Hilfsmittel als die angegebenen benutzt worden sind und dass die Stellen der Arbeit, die anderen Werken – auch elektronischen Medien – dem Wortlaut oder Sinn nach entnommen wurden, auf jeden Fall unter Angabe der Quelle als Entlehnung kenntlich gemacht worden sind.

____

(Datum, Unterschrift)

Ich erkläre mich mit einem Abgleich der Arbeit mit anderen Texten zwecks Auffindung von Übereinstimmungen sowie mit einer zu diesem Zweck vorzunehmenden Speicherung der Arbeit in einer Datenbank einverstanden.

____

(Datum, Unterschrift)

Contents

1. Introduction **7**

2. Dark Matter and the XENON Dark Matter Project **9**
2.1. Dark Matter 9
2.1.1. Bullet Cluster 9
2.1.2. Cosmic microwave background radiation 9
2.1.3. WIMPs as Candidates for Dark Matter 10
2.2. The XENON Dark Matter Project 10

3. Münster's Dual-Phase Time Projection Chamber **13**
3.1. General Setup of a Dual Phase Xenon TPC 13
3.2. The Münster TPC setup 15
3.3. Data Acquisition and Processing 15
3.4. PAX - Processor for Analyzing Xenon Data 18

4. PMT Characterization and Calibration with an LED **21**
4.1. LED Output Intensity Development 21
4.1.1. LED gain calibration 23
4.1.2. Using LED data for Setting Thresholds 27
4.1.3. Camparison to Fixed Window Integration Method 29
4.1.4. Problematic Channels 32

5. Kr83m Measurements in a Single Phase Gaseous TPC **35**

6. Dual phase Measurement with a ^{137}Cs Source **39**

7. A Magnetically Driven Piston Pump **41**
7.1. Outer Frame and Drive 43
7.2. Gas Line Setup 44
7.3. Leakage Measurements 44
7.3.1. Piston Gaskets 44
7.3.2. Flapper redesign 47
7.4. Calculation of XENON pump performance 50
7.4.1. Performance Measurements 55
7.4.2. Long Term Test 59

8. Summary and Outlook **65**
8.1. Münster TPC 65

8.2. Xenon Pump 65

9. Bibliography 67

A. Appendix 71

1. Introduction

Astrological observations showed that only the minority of the universe's energy density can be described with standard model particles. With almost 70%, the majority of the universe consist of "dark energy", which is still of unknown nature. The remaining 30% are made of mass. However, the proportion of this mass is in big conflict with the matter seen in night sky. A solution to this mystery is the assumption of invisible mass which is expediently called "dark matter". It has been found out that dark matter makes up 25% of the universe's energy density, leaving about 5% to standard model particles. The presence of dark matter has been proofed by several cosmological observations which can hardly be explained without the assumption of additional matter.
Furthermore, dark matter does not share particle interactions in the same way as standard model particles. Due to the strength of electromagnetic and strong interaction it could be ruled out that dark matter does interact via these forces. In fact, it is not known whether dark matter does interact with ordinary matter at all.
However, interactions at the scales of weak interaction are suggested by some theories. A predicted group of particles are the so called WIMPs, the "weakly interacting massive particles". The search for these particles is a recent topic of research. Several international experiments are looking for signs of WIMPs, but have yet only been able to set upper limits for their cross-section. A detector type that has been used in the recent years for direct dark matter search are dual phase time projection chambers (TPC). In order to develop new techniques and understand the behavior of such detectors, a TPC has been built in Münster. In this thesis, tests and measurements on this setup are presented, as well as the implementation of a new raw data processor.

The second topic in this thesis is the follow-up development of a pump to be used in high-purity xenon experiments like XENON1T or the neutrinoless double beta decay experiment EXO. As bellows pumps or diaphragm pumps cannot ensure containment in the case of failure, a piston pump type was chosen. In order to fulfill the extreme requirements, the piston is driven within a sealed container. This requires a magnetic transmission of force between the piston and the motor.
After a detailed description of the setup and the redesigns of two essential components, performance test are presented in this thesis.

2. Dark Matter and the XENON Dark Matter Project

2.1. Dark Matter

Cosmological observations in the last century changed the predominant image of our world like no other. It became clear, that the majority of our universe consist of two former unknown components. Today, these components are known as dark energy and dark matter. While dark energy is responsible for the accelerated expansion of our universe, dark matter is an explanation for several astronomical observations. These observations are based on gravitational effects, which can not be explained by visible (or ordinary, baryonic) matter alone. Instead, dark matter has to consist of neutral, massive particles. Though neutrinos also contribute to the proportion of dark matter, their lightweight masses rule out the option to be the only explanation for dark matter. Different theories like MACHOs[1] or MOND[2] do not solve the missing mass problem satisfactorily either.

2.1.1. Bullet Cluster

The possibly most appealing evidence for dark matter are observations of the Bullet Cluster[1]. This object of two galaxy clusters which have collided in the past, as shown in fig. 2.1, indicate that the stars are not vastly disturbed by this astronomical impact. Instead, they pass rather unnoticed, as the distances of the solar systems are still monumental. After careful observation of gravitational lensing, it was found that the centers of mass of both galaxy clusters align with the observed stars.

However, if there was no dark matter, the majority of the mass in the galaxy clusters would originate not from stars and planetary objects but from gas clouds. These can be observed with X-ray telescopes. Due to their higher interaction with one another, the respective gas clouds from both galaxy cluster slowed down during the collision. The mismatch between this expectation and the observation can be explained by additional mass which does not participate in the collision either.

2.1.2. Cosmic microwave background radiation

The most accurate results for the composition of our universe comes from the Planck experiment[2]. From these results it is known that we most likely live in a flat universe.

[1] Massive astrophysical compact halo object
[2] Modified Newtonian Dynamics

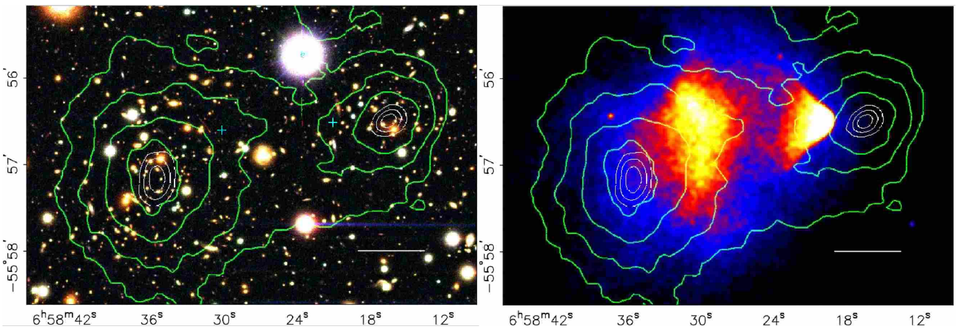

Figure 2.1.: Picture of the bullet Cluster. Left: optical image, right: X-ray spectrum. The name comes from the conical shape of the smaller galaxy cluster in the X-ray spectrum. Overlayed in both images is the observed mass distribution according to gravitational lensing analysis. [1]

Furthermore, it has been found that the majority of the universe consists of dark energy. At a confidence level of 1σ, the cosmological parameters can be received by fitting the ΛCDM model to the cosmological observations. The results are shown in table 2.1.

Table 2.1.: Cosmological composition of the universe from [2]

Ω_Λ	0.6911 ± 0.0062
Ω_m	0.3089 ± 0.0062
$\Omega_{m,\text{dark matter}}$	0.2589 ± 0.0057
$\Omega_{m,\text{baryonic matter}}$	0.0486 ± 0.0010

2.1.3. WIMPs as Candidates for Dark Matter

Dark matter could be composed of particles which only interact with standard model particles gravitationally and via a force on scales of the weak nuclear force. A predicted class of particles are weakly interacting massive particles, or WIMPs. Furthermore, it presumably must not interact with baryonic matter via electromagnetic or strong interaction, as it would already have been detected otherwise. So far, no WIMP has been observed and only upper limits for its cross-section could be given. The most recent limit was given by the LUX collaboration to be $0.6 \times 10^{-45}\,\text{cm}^2$[3] for $33\,\text{GeV}/\text{c}^2$.

2.2. The XENON Dark Matter Project

With the XENON1T experiment[4], the XENON collaboration started into the third stage of its direct dark matter search. Its predecessors XENON10[5] and XENON100[6] have set upper limits for the WIMP-nucleon scattering cross section down to $2 \times 10^{-45}\,\text{cm}^2$ for $55\,\text{GeV}/\text{c}^2$ and 90% confidence level [7]. After XENON1T's commissioning phase, the experiment is designed to probe WIMPs down to a cross section of $1.6 \times 10^{-47}\,\text{cm}^2$ for

$50\,\mathrm{GeV/c^2}$ [8].
The detector type is a dual phase time projection chamber (TPC) and is located in the Hall B of the Laboratori Nazionali del Gran Sasso. The working principle of this detector type is explained in the chapter about the Münster TPC(see section 3.1).

The cylindrical detector has an inner diameter of 104 cm and a height of 107 cm. After ongoing tests of several subsystems, the detector will be filled with approximately 3 tonnes of liquid xenon, of which approximately 1 tonne is the fiducial target mass. The PTFE covered inner cylinder is kept under observation by 248 individual photomultiplier tubes[3]. Furthermore, the cryostat is contained in a water tank of 10 m in diameter. Photomultiplier tubes in this shielding allow the detection of muons, thus providing an active shielding for the TPC.

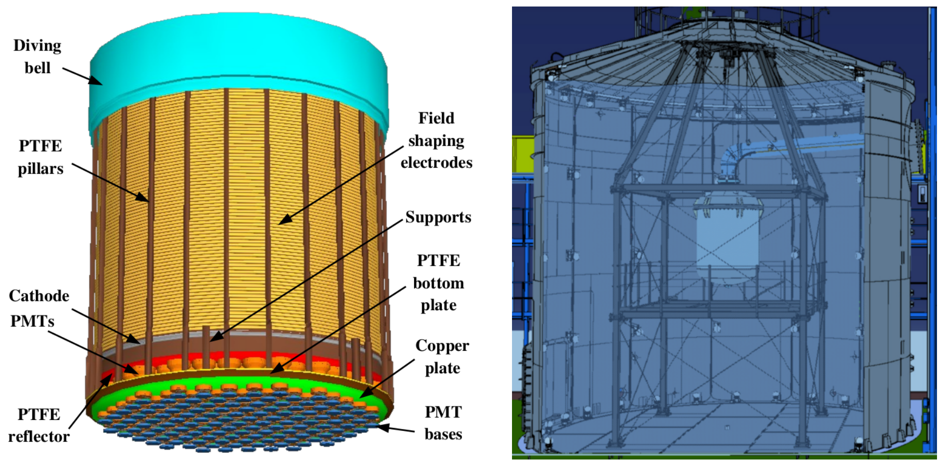

Figure 2.2.: Left: CAD drawing of XENON1T TPC from GEANt4 simulation. Right: Water tank with the cryostat in the middle. The water tank is equipped with photo multiplier tubes in order to act as an active muon veto. [8]

[3] Hamamatsu R11410

3. Münster's Dual-Phase Time Projection Chamber

3.1. General Setup of a Dual Phase Xenon TPC

TPCs are broadly used in particle and astro-particle physics as a detector for a wide range of particles. Using a detector volume of a gas or liquid, in combination with an electric field, TPCs are rather easy to scale, while still giving a three-dimensional reconstruction of a particle incident. Liquid dual phase TPCs are a special type of time projection chambers, as they have a liquid *and* a gaseous phase of a noble gas. Within the liquid, and thus dense phase, the mean free path for a particle is orders of magnitude less than in the gaseous phase.

The working principle of a dual phase is shown by the example of the Münster TPC in fig. 3.1. When an incoming particle scatters at an atom (nucleus or electronic shell), the prompt scintillation light (S1 signal) is measured by the PMTs. These are located at the top and bottom of the cylindrical detector. Due to the phase transition between liquid and gaseous phase, the S1 signal is primarily measured by the bottom PMTs. Simultaneously, ionization of the noble gas atoms produces free electrons that, under the influence of an electric field, drift with a constant velocity(see [9] fig. 10) towards the surface [10]. The electric drift field is created by a high voltage between the cathode at the bottom and a gate mesh on ground potential. In order to provide a homogenous shape of the field, copper rings that are connected via a resistor chain, are mounted into the cylinder wall. Once the electrons reach the transition, they are accelerated in the gaseous phase by another electric field towards the anode. During their mean free paths, they gain enough energy to excite the gaseous atoms, thus producing light again (S2 signal). This is proportional to the number of electrons and to the anode voltage. The level of the liquid surface has to be regulated with little fluctuations, as otherwise the amplification differs over time. Furthermore, if it the level is not exactly between the gate mesh and the anode, no S2 signal is produced at all.

The underlying processes of the signals S1 and S2 are excitation and ionization respectively[11] and apply for argon, krypton and xenon similarly. Following, the process is described by the example of xenon. The S1 signal is created by an *excimer* (excited dimer) of xenon [10].

$$\chi + \mathrm{Xe} \rightarrow \chi + \mathrm{Xe}^* \tag{3.1}$$

$$\mathrm{Xe}^* + \mathrm{Xe} + \mathrm{Xe} \rightarrow \mathrm{Xe}_2^* + \mathrm{Xe} \tag{3.2}$$

$$\mathrm{Xe}_2^* \rightarrow 2\mathrm{Xe} + h\nu \tag{3.3}$$

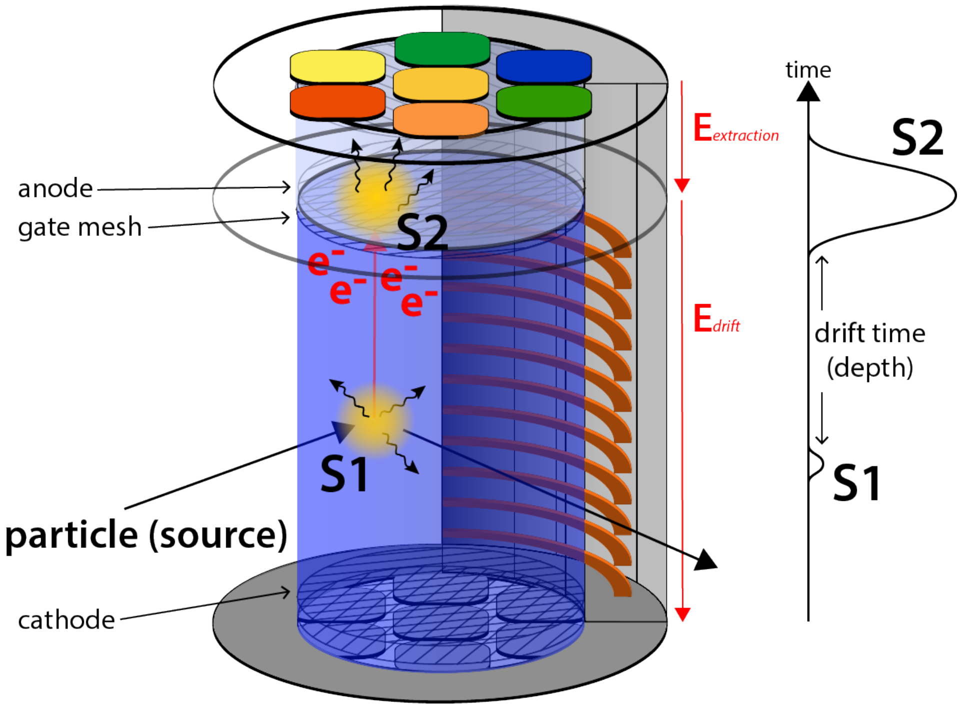

Figure 3.1.: Sketch of the Münster TPC. Image by [12]

As shown, χ is the incoming particle and $h\nu$ represents the prompt scintillation photon with the characteristic wavelength (in liquid) of 178 nm. Alternatively, ionization can occur. In this case an electron becomes free. This can recombine with the ionized xenon atom by following scheme.

$$\chi + \mathrm{Xe} \rightarrow \chi + \mathrm{Xe}^{+} + \mathrm{e}^{-} \tag{3.4}$$

$$\mathrm{Xe}^{+} + \mathrm{Xe} \rightarrow \mathrm{Xe}_2^{+} \tag{3.5}$$

$$\mathrm{Xe}_2^{+} + \mathrm{e}^{-} \rightarrow \mathrm{Xe}^{**} + \mathrm{Xe} \tag{3.6}$$

$$\mathrm{Xe}^{**} \rightarrow \mathrm{Xe}^{*} + \mathrm{heat} \tag{3.7}$$

The Xe^{*} in eq. (3.7) eventually emits a photon according to the process described in eq. (3.2). This way, the ionization process with the following recombination contributes also to the S1 signal. However, the electron can be extracted via an electric field in which it moves with a constant velocity towards the anode - or more precisely - to the gate mesh (see fig. 3.1). With the surface of the liquid phase being at the gate mesh, the space between anode and gate mesh is in gaseous phase. Here, the electrons do not move with constant velocity anymore. Instead, they get accelerated to energies in which they can excite themselves xenon atoms. The collected light of this process is referred to the S2 signal.

3.2. The Münster TPC setup

The Münster TPC was built in 2011 [13] and has a 4 cm inner radius and is 17 cm high (maximum drift length). Thus, it can contain up to ≈ 2.6 kg of xenon as its active detector material. The drift field is shaped homogeneously by 12 copper rings connected via a resistor chain. For high reflectivity[14] in the VUV spectrum, the inner wall of the cylindrical detector is made of PTFE.

The detector volume is observed by 14 PMTs, proportioned 7 on the top and bottom respectively. The arrangement is shown in fig. 3.2.

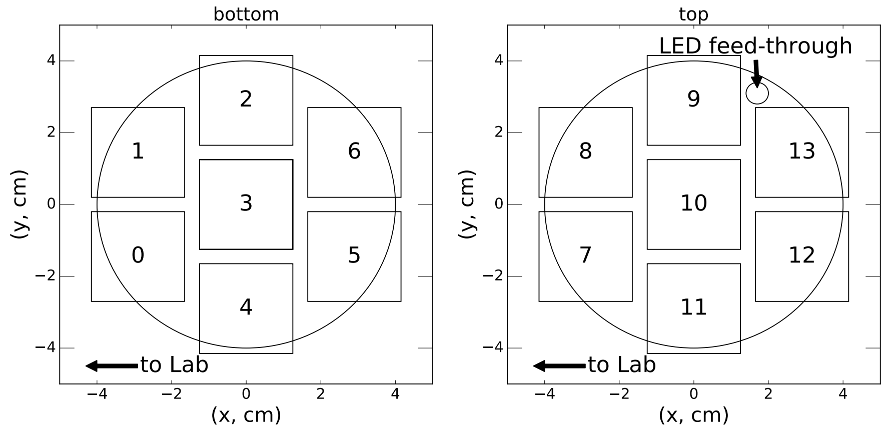

Figure 3.2.: PMT pattern of the Münster TPC for top and bottom array. Additionally, the inner TPC radius is marked.

3.3. Data Acquisition and Processing

Data taken by the CAEN® 1724 flash ADCs are stored with the software FPPDAQ by Volker Hannen. Basically, FPPDAQ is responsible for the control of the connected boards. It also handles the file I/O and writes metadata for each file and event respectively. The data structure of the actual data is predetermined by the flash ADCs themselves. A detailed description of an event file (*.eve) can be found in the appendix. This knowledge is vital in order to write an input plugin for the raw data processor.

The flash ADCs map a voltage range of 0 V to 2.25 V onto ADC units with 14-bit precision. The number of electrons can be calculated using the factor $N_{\text{ADC to e}}$ from eq. (3.8).

$$N_{\text{ADC to e}} = \frac{\langle\text{sample duration}\rangle\,\langle\text{voltage range}\rangle}{\langle\text{PMT resistor}\rangle\,\langle\text{digitizer bits}\rangle\,\langle\text{external amplification}\rangle\,\langle\text{electron charge}\rangle} \tag{3.8}$$

Here, all factors are known, but in part dependent on the flash ADC model/settings and the PMT model. In short, the factor can be summed up to:

$$N_{\mathrm{ADC\ to\ e}} = 17\,143\,\mathrm{e}^{-}/\mathrm{ADC\,unit} \tag{3.9}$$

There are two different modes, dependent on whether the measurement is supposed to be performed in TPC mode or the LED is used (see fig. 3.3). In the former case, the flash ADCs are using their internal thresholds. The boards then give a *trigger out* signal to an Fan in/Fan out in logic or mode. From this, the output signal is going to the *trigger in* ports of both boards. With that, the boards are synchronized and record signals without any time difference.

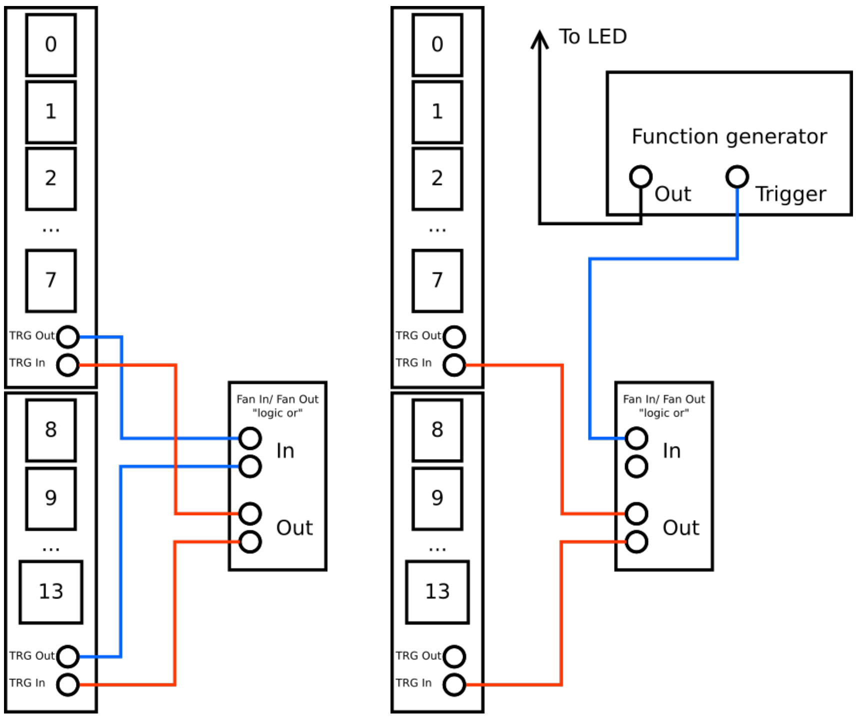

(a) TPC mode (b) LED mode

Figure 3.3.: Wiring of flash ADCs for TPC mode and LED mode.

In the second case an internal triggering is undesirable as they might come from muons, or even likelier electronic noise. Instead, the flash ADC boards are triggered by the function generator which triggers the LED as well. For gain calibration, this makes the mandatory thresholds obsolete. In chapter 4 it will be shown, how the measurement will be performed in detail.

First, some technical terms have to be introduced, as they are crucial for proper measurements. They are needed to adjust the CAEN1724 boards correctly.

(Triggering) Threshold In TPC mode, a triggering threshold has to be set in ADC units. When this threshold is overstepped an event of a fixed length (see *page size*) will be stored. Thus, an event has always a fixed size.

Page size The number of samples for each event and channel are preset by the page size. It amounts between 2^8 and 2^{19} samples.

Post trigger samples This number sets the position of the trigger in each event by the number of the following samples. It can be set in a way, that the largest (most likely S2) signal is close to the end of the events, so that the beforehand S1 signal are found in earlier samples. In the actual implementation the **trigger time** is set indirectly by this value and the page size.

Zero suppression Zero suppression is a technique to limit the logged data to a relevant fraction. Non-contributing PMTs are not stored. Furthermore, not all samples of contributing channels are logged, either. Instead, the zero suppression threshold has to be exceeded.

Zero-suppression-threshold This threshold is also set in ADC units and determines whether a given channel's data are stored. If all samples are below this threshold, the channel does not contribute at all to this event. When one sample exceeds the threshold, this and a given number of samples before and after are logged. The exact number can be set by the *zle_nlbk* (number look back) and *zle_nlfwd* (number look forward) parameter. A systematic approach to set the zero-suppression-threshold value reasonable is presented in section 4.1.2.

3.4. PAX - Processor for Analyzing Xenon Data

PAX is a raw data processor developed by the XENON collaboration for analyzing dual phase TPC data. The existing raw data processor XeRawDP, which has been used for XENON100, did not fulfill the needs for the next generation experiment XENON1T. The goal was to create an improved processor in terms of noise handling, peak identification and usability. Also, it was developed from scratch in the programming language Python3[1], while XeRawDP was written in C++. This has been done mainly by the collaboration members at Nikhef(NL), primarily by C. Tunnel and J. Albers.

It was jumped at the chance to create a raw data processor that is not only designed for the XENON1T TPC or upcoming successors. Instead, the software was designed modularly to fit for all sizes of dual phase TPCs. This approach allows the adaption to smaller setups like the Münster TPC. The data processing is done by several plugins, each dedicated to a certain step in processing.

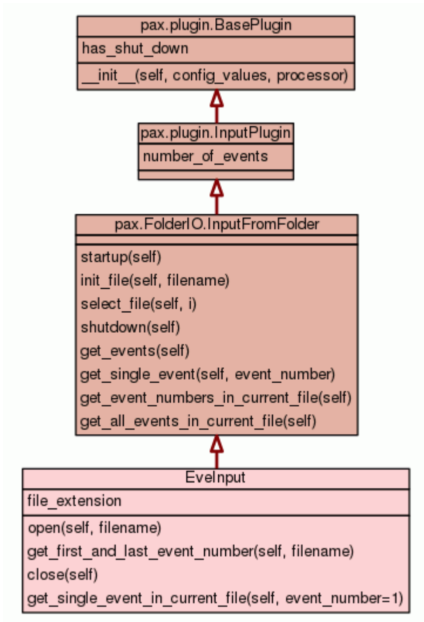

Figure 3.4.: UML diagram of the EVE_file.py plugin

In order to use PAX on Münster TPC data, two things had to be created: Firstly, an input plugin for the *.eve file format, and secondly, a configuration file [2]. The input plugin needed to fulfill the compatibility requirements of the FolderIO base class (see fig. 3.4).

All plugins that need custom settings are configured by a configuration file. For all measurements, these parameters will be added to the appendix.
This configuration file also includes a list of classes which are transforming the data. As plugins can use data of other plugins, they have to be called in the right order. An example for the analytical structure is shown in fig. 3.5. From bottom to top, the data is combined until eventually it becomes a reconstructed interaction. A detailed description of the analysis is presented later. At this point, the data structure should be in focus as the terms used are recurring in later chapters.

Event This includes all data that was taken during a trigger. It contains all samples from all (or, if ZLE is enabled, all contributing) channels and also time information. Within

[1] `www.python.org`

[2] Further information about the Münster TPC (e.g. an energy correction based on a light collection efficiency map) are required by some plugins and have thus to be available as well.

PAX, an instance of the *Event* class also contains objects with additional/processed information.

Pulse Each channel of the FlashADC boards continuously takes samples at a set sampling frequency (for example $\frac{1}{10\,\text{ns}}$). When the FlashADC is triggered, a predetermined number of samples in all channels before and after this triggering sample stored (see section 3.3). Multiple pulses for the same channel in a single event (e.g. separated by ZLE) are treated as independent pulses.

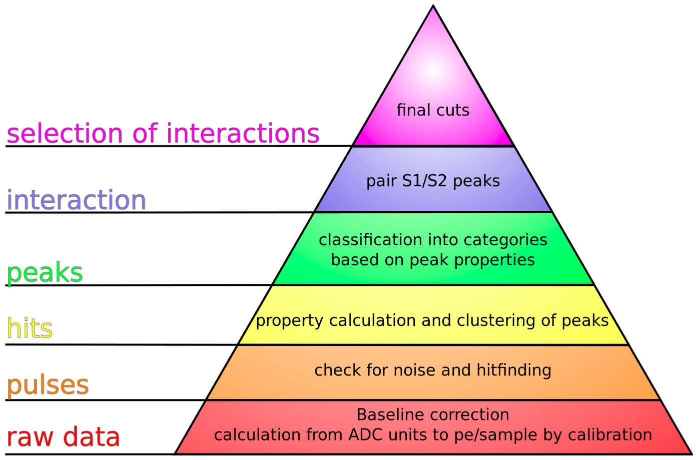

Figure 3.5.: Step-by-step process of reconstructing initial interaction by several layers of transformation.

Hit The individual pulses are analyzed for samples that exceed the baseline which is determined by the average of the first samples (number can be adjusted) of each pulse. Afterwards, these samples are stored as a hit. The exceeding of the waveform has to pass a threshold which is calculated for each pulse (more details are described in section 4.1.1).

Peak Hits that are likely to have the same origin are clustered into a peak. Which hits are accepted to contribute to a peak, are determined by clustering algorithms. After clustering, peak properties are calculated which correspond to desired physical information, e.g. deposited energy, width, xy-reconstruction etc.

Interaction Are both, an S2 and an S1 peak identified within a single event, these peaks are paired to an interaction. As usually more peaks than these two are present within an event, the most likely peaks for a common origin are paired. Also, the z-position and the 3D origin of the physical incident can be determined as it can be calculated with the aid of the time difference of both peaks. Now, most of the remaining properties(corrections for travel time, light collection efficiency etc.) can be calculated, as many of them require the 3D-position of the original scattering.

4. PMT Characterization and Calibration with an LED

For understanding the performance of the Münster TPC, a proper characterization of the 14 individual PMTs is crucial. This can be done using an LED which is coupled into the TPC via a glass fiber[15]. Apart from the gain calibration, which is likely to be the most important use of the LED, this upgrade allows a range of new measurements which were not possible offhand before.
The aim for the gain calibration is to have a well-known amplification for the photo electrons for each channel.

4.1. LED Output Intensity Development

All tests with the LED are performed by using a signal generator Tektronix AFG 3102 [16] which simultaneously triggers the CAEN1724 flash ADC boards and turns on the LED (see fig. 3.3b). By turning on the LED, after a delay of 1 μs, the first 100 samples of the event can be used for determining the baseline and noise. As the trigger time was set to be 1 μs within the event, the LED is turned on at the 2000 ns positions of the recorded events. However, the assumption that the LED responds quick enough during the rest of the measurement window needs to be confirmed. By that, the LED's output intensity in reliance on time can be measured simultaneously.

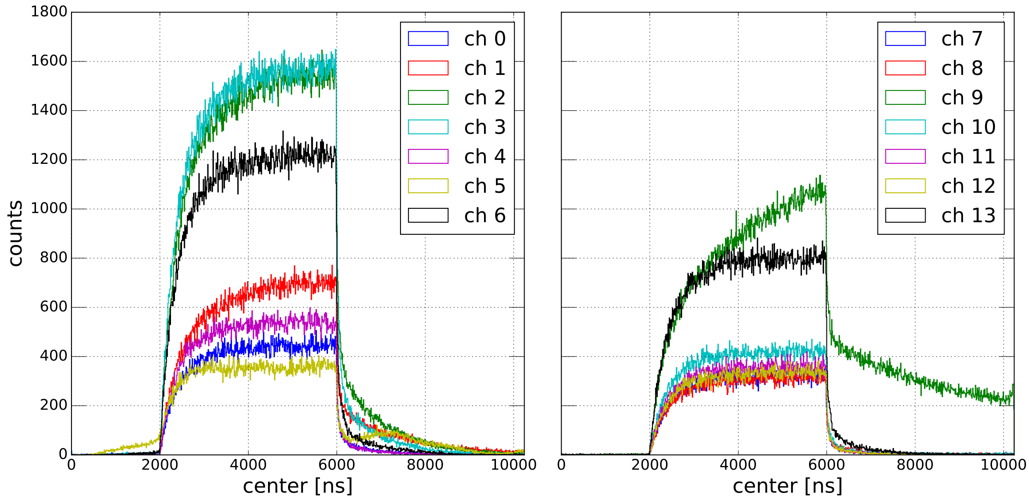

Figure 4.1.: Hits versus time of individual PMTs (left: bottom, right: top). Data was taken using a 10 240 ns wide window with all PMTs supplied by an equal high voltage of 850 V. The trigger time was set to 1000 ns, and the LED was turned on with 970 mV after a delay with respect to the trigger of 1000 ns for 4 μs. The pulsing frequency was at 100 Hz. Measurements were taken at room temperature.

In fig. 4.1 a histogram of the hits' centers is shown. The property *center* is calculated by PAX and resembles the mean time of a hit within its event. On average, 37.76 hits have been found per event. The plot shows a rise in all channels after 2000 ns. For most channels, the rate stabilizes within 1000 ns to 2000 ns. As the bottom PMTs are illuminated directly through the glass fiber on the top of the PMTs, there is a trend to higher rates in comparison to the top PMTs, which are only light up by reflections. After 6000 ns, when the LED was turned off again, the number of counts drastically decreases in all channels. However, after the turn off virtually all channels still do have hits.
This pattern is broken for channel 9, which first rises indefinitely, until the LED is turned off. After that, the rate is still almost half as high as immediately before the LED power off, and then slowly decreases until the end of the measurement window. For the next repetition, which begins after 10 ms at the set rate of 100 Hz, the rate has dropped to zero, as there would be a noticeable amount of counts before the 2000 ns mark otherwise. This effect in channel 9 is not negligible, as the count ratio between the number of hits with a center higher than 6100 ns, and the number of total hits is way higher than for all other channels (see table 4.1). So far, the actual reason for this "after-pulsing" remains unclear. Different properties like "height", "area", or "width" of these after-hits were indistinguishable from the correlated hits. However, decreasing the high voltage for this channel, this effect vanishes to an equal amount like seen in the other channels.

Table 4.1.: Number of total hits and hits after turning off the LED.

channel	# of total hits	# of hits with center > 6100 ns)	$\frac{\langle \text{hits with center}>6100\,\text{ns}\rangle}{\langle \text{total hits}\rangle}$
0	163 680	4422	0.03
1	264 029	24 706	0.09
2	572 179	33 060	0.06
3	578 776	19 579	0.03
4	197 144	3875	0.02
5	158 572	18 660	0.12
6	445 981	9379	0.02
7	117 568	2133	0.02
8	115 947	3894	0.03
9	462 162	129 333	0.28
10	154 459	3933	0.03
11	130 930	2107	0.02
12	122 343	2068	0.02
13	292 434	6512	0.02

The different counts of hits can be a hint for relative differences in quantum efficiency. However, it cannot be more than that, as other effects like shadowing of the PMTs(see fig. 3.2) and the not known illumination by the LED will have an effect as well.

4.1.1. LED gain calibration

A method for gain calibration has been presented in [15]. Here, another approach will be suggested, using the hit-finder of PAX . Both methods will then be compared. In the next chapter it is shown how further information can be used to find reasonable parameters for measurements with internal triggering and zero suppression.

For calibration, the installed glass fiber can be used to illuminate the PMTS with various light sources. As the quantum efficiency is not important for the gain calibration, the following measurements were performed with the same LED as above. The gain itself should not be dependent on the wavelength, except for effects that will be neglected here (for example the possibility of two primary emitted photo electrons by a single photon).

The established procedure for calibration is to integrate the waveform for a certain number of samples. The LED voltage or the size of the window have to be chosen in a way that the probability for a single photo electron (pe) is about 5%. In practice fixing a window of about 20 samples and adjusting the LED voltage accordingly was more reliable than sizing the window to the data. Of course, setting the voltage has to be repeated for every PMT due to different quantum efficiencies and local illuminations via the glass fiber. Otherwise, the ratio between zero-, one-, and two-pe's in the window might vary too much, causing problems when trying to fit respective peaks to them.

A new idea for calibration uses a different approach. The basic idea is to have a method that makes use of PAX 's hit-finder. In the following, the working principle of this hit-finder will be outlined. Unlike the method briefly summed up above, the integration window is not fixed, but adapts to the samples of each pulse with the use of a hit-finder. Before the procedure will be described in detail, the main advantages of this approach are pointed out:

- Doing the calibration differently as PAX determines the number of photo electrons could result in a systematic difference while processing. If PAX itself introduces a bias, this could cancel out when the calibration is done the same way.
- As identified hits are usually 3 or fewer samples long, the density of single pe signals can be higher. This means, the LED can be driven at a higher voltages. This was not possible with the established method as multiple photo electrons could not be separated properly. At too high intensities, the determined gain would eventually differ as the separation will also fail at some point due to pileup of hits.
- A randomly "cut-off" of actual hits in between, when they are at the very beginning or end of the fixed-window cannot happen. However, choosing the *upper* and *lower threshold* correctly (see below) is important and can bias the result.
- In table 4.1 can be seen, that between 100 000 to 500 000 hits per channel can be extracted out of 100 000 events for the used LED voltage. Thus, the same data file can yield way higher statistics.

For the third point, it can be argued that it the issue is negligible . On average, single pe signals are made up of less than two samples (see fig. 4.4). Also, the last argument can be bypassed by a longer measurement time, and an advanced implementation of the calibration software. For the current fixed-window program, only a single window per event and channel is used, leaving the remaining 95% of the relevant samples unused.
However, the first two reasons are systematic. It might be possible, that the second argument has another advantage as a result, when discussing problematic channels. Nevertheless, the working principle of this approach has to be explained in detail.

Working Principle of PAX 's Hit-Finder

The data, which does not differ from data used for the established method (zero suppression off), is normally read into PAX with a dedicated configuration file (see appendix). With that, only necessary classes are loaded and for other purposes expandable low-level data is stored. The LED is set to voltages from 960 mV to 1000 mV. In the first n samples[1] the baseline will be determined by the mean.

Simultaneously the noise σ of the baseline samples is quantified by eq. (4.1). This value is responsible for the dynamic hit-finding thresholds.

$$\sigma = \left(\frac{1}{n} \sum_{i=1}^{n} \left(\langle \text{baseline} \rangle - x_i \right)^2 \cdot \Theta \left(\langle \text{baseline} \rangle - x_i \right) \right)^{\frac{1}{2}} \tag{4.1}$$

[1] number can be set in the configuration file in section **[HitFinder.FindHits]** → **initial_baseline_samples**

In eq. (4.1) Θ is the Heaviside function, and x_i are the single uncorrected samples (negative signals w.r.t. baseline). Although the signals are negative as they represent a charge of electrons, from here it is functional to flip the sign. This is done within PAX during the baseline subtraction. Hits and peaks in the following plots of waveforms will thus be positive.

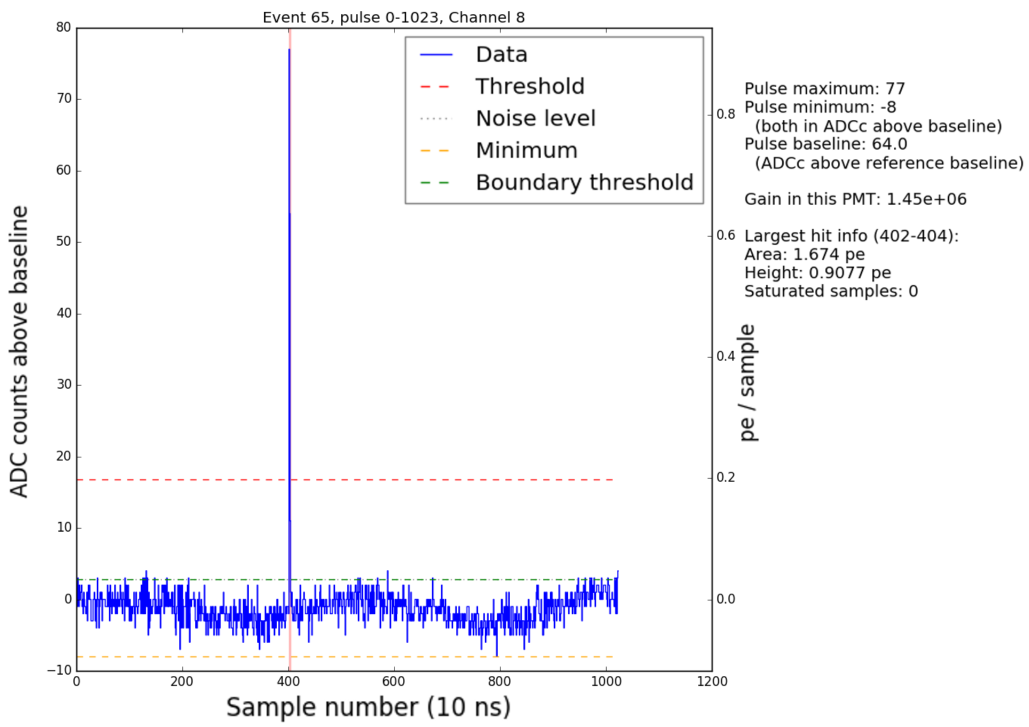

Figure 4.2.: Diagnostic plot created by PAX . The *height_over_noise_low_threshold* (here *Boundary threshold*) was set to 1σ and the *height_over_noise_high_threshold* (here *Threshold*) was set to 3σ. A single hit was found with an area of 1.674 pe (according to the respective gain calibration).

An exemplary pulse is illustrated in fig. 4.2. After the calculation of baseline and noise sigma, the hit-finding algorithm looks for samples in each pulse, which exceed the baseline by the *height_over_noise_low_threshold*. Along with that, a *height_over_noise_high_threshold* has to be set in the configuration file for PAX . These thresholds are set in multiples of the above calculated σ. If now a certain sample exceeds the limit of the *low_threshold* (e.g. 1σ), the hit-finder starts adding up the following samples until one sample falls below this threshold again. These samples will be stored as a hit, if the *high_threshold*(e.g. 3σ) was crossed in between. Otherwise, the samples will be discarded and the hit-finder continues with rest of the pulse. As the noise σ is calculated for each pulse, randomly occurring noise in one channel will dynamically increase the necessary height for a signal to be considered. With that, noisy channels can be filtered out more reliable than with static thresholds (see section 4.1.4).

Calibration of PMTs

When the hits have been found, some additional properties are calculated. For the gain calibration, the area is used, as it is proportional to the produced charge in the PMT and thus to the number of the initial photo electrons. The area of all hits can be plotted into a histogram. This can be seen for all channels in fig. 4.3.

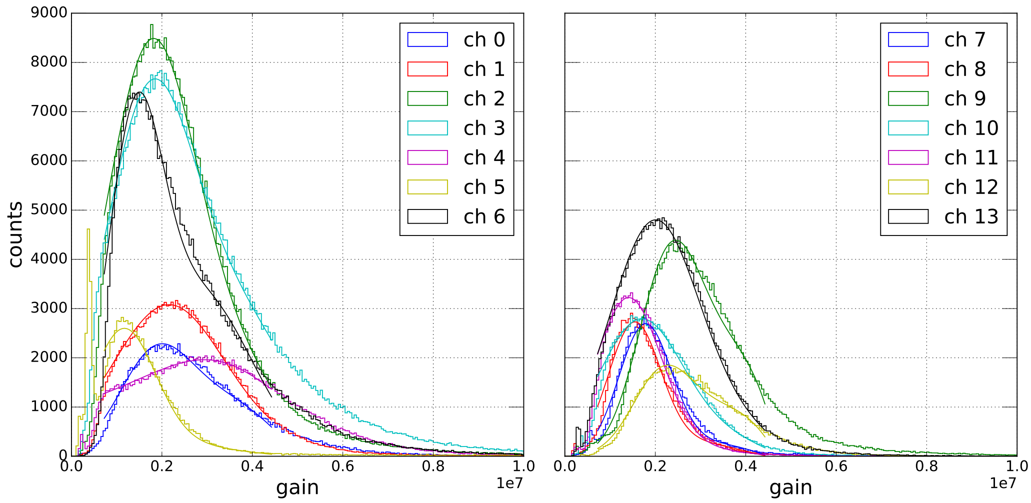

Figure 4.3.: Histogram of area for all channels. Left: bottom PMTs, right: top PMTs

The function used for fitting the data is considering three Gaussian functions with independent amplitudes:

$$f(x) = A \cdot e^{-\frac{1}{2}\cdot\left(\frac{(x-\text{gain})}{\sigma}\right)^2} \tag{4.2}$$
$$+ A_2 \cdot e^{-\frac{1}{2}\cdot\left(\frac{(x-2\cdot\text{gain})}{2\cdot\sigma}\right)^2} \tag{4.3}$$
$$+ A_3 \cdot e^{-\frac{1}{2}\cdot\left(\frac{(x-3\cdot\text{gain})}{3\cdot\sigma}\right)^2} \tag{4.4}$$
$$\tag{4.5}$$

The parameters "gain" and "σ" are not independent, because that would not represent the physical working principle of a PMT.
In most channels, the first Gaussian peak has the highest amplitude followed by decreasing peaks. This represents the signal coming from single photo electrons. Double or multiple photo electron peaks are occurring less frequently. Channel 5 is here an exception. The first peak at a gain of $\approx 4 \times 10^5$ is likely to have a different physical origin. Later in

section 4.1.4, channel 5 will be looked into deeper. The gains and errors obtained out of the fits are shown in table 4.2.

Table 4.2.: Gains determined for each channel

Channel	Gain [10^6]	σ [10^6]
0	1.834 ± 0.011	0.769 ± 0.010
1	2.145 ± 0.045	1.223 ± 0.024
2	1.739 ± 0.008	0.974 ± 0.009
3	1.694 ± 0.010	0.940 ± 0.011
4	3.818 ± 0.385	1.618 ± 0.489
5	1.175 ± 0.008	0.701 ± 0.007
6	1.423 ± 0.004	0.595 ± 0.004
7	1.797 ± 0.003	0.578 ± 0.003
8	1.556 ± 0.003	0.576 ± 0.003
9	2.335 ± 0.006	0.695 ± 0.004
10	1.662 ± 0.008	0.897 ± 0.011
11	1.425 ± 0.005	0.722 ± 0.005
12	2.169 ± 0.008	0.658 ± 0.005
13	1.978 ± 0.011	0.968 ± 0.009

4.1.2. Using LED data for Setting Thresholds

Measurements with internal sources cannot be triggered coincidental as it was shown for the LED measurements. Instead, internal triggers have to be used. For this purpose, the signal for a given channel has to exceed a certain threshold to trigger the data acquisition. In order to limit the amount of data, zero suppression is used. This technique limits the data acquisition to channels, which are contributing a signal.

In order to decide whether that is the case, a lower threshold called the zero suppression threshold has to be set. Channels that are exceeding this value are stored even if they are not high enough to trigger. Unlike the hitfinding algorithm in PAX, these two thresholds have to be set in absolute ADC units and not in relative values compared to the noise. Thus, individual baselines and thresholds have to be determined for each channel.

If the thresholds are too low, it could cause the flash ADC boards to become busy due to an extreme event rate. If they are too high, information gets lost. While the triggering threshold is only limiting the amount of events to those which include at least one channel with a high sample, the zero suppression threshold is responsible for cutting low signals. Ideally, it is set so that all single photons are recorded. As the gain is individual for all PMTs, the thresholds will also be gain-dependent. Furthermore, a different transit time spread[2] could lead to channels with a lower height, but with a higher width

[2]The transit time spread is the fluctuation of the time between the emission of the primary photo electron and the detection of the PMT's anode.

instead. To test this, the height versus the area can be plotted, which is shown in fig. 4.4 on the example of channel 7.

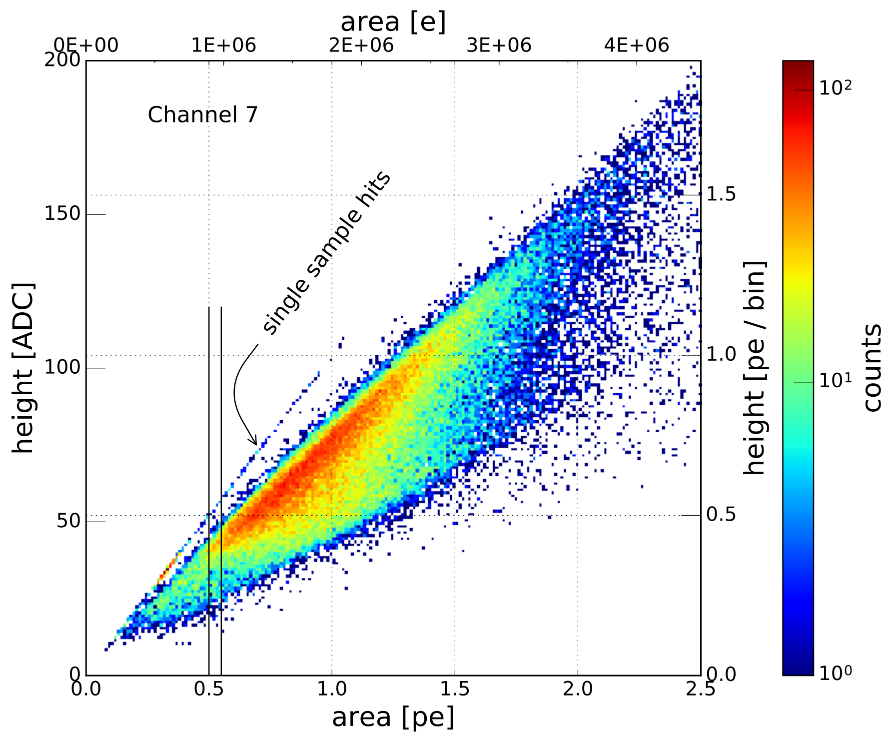

Figure 4.4.: Height versus area on the example of channel 7. Hits consisting of only a single sample build a distinct line with the highest possible slope. Most hits have a dominant and a minor sample, which can be seen at the accumulation close to this distinct line. Furthermore, the area from 0.5 to 0.55 pe is marked, which contains hits for the threshold determination.

What can be seen here is a high correlation between height and area as it was expected. Furthermore, it can be seen that there is an accumulation close to the line of single-sample hits. This means that the contribution to a hit comes mainly from a single sample, while the other(s) make(s) only little amount towards it. In fact, most hits have a ratio between the main contributing and all other samples of more than 2 to 1.

Now, the desired threshold can be chosen in units of pe. In fig. 4.4 the area between 0.5 pe to 0.55 pe is marked. Hits in this selection can be filled into a histogram, which is shown in fig. 4.5. The mean or the median will be the zero suppression threshold with respect to the baseline. Choosing a lower value, would result in more and more noise that would be recorded. Whether 0.5 pe is a good choice for a threshold will need further investigation. Furthermore, a physically sound fitting model may be desirable. This procedure has to be repeated for every channel.

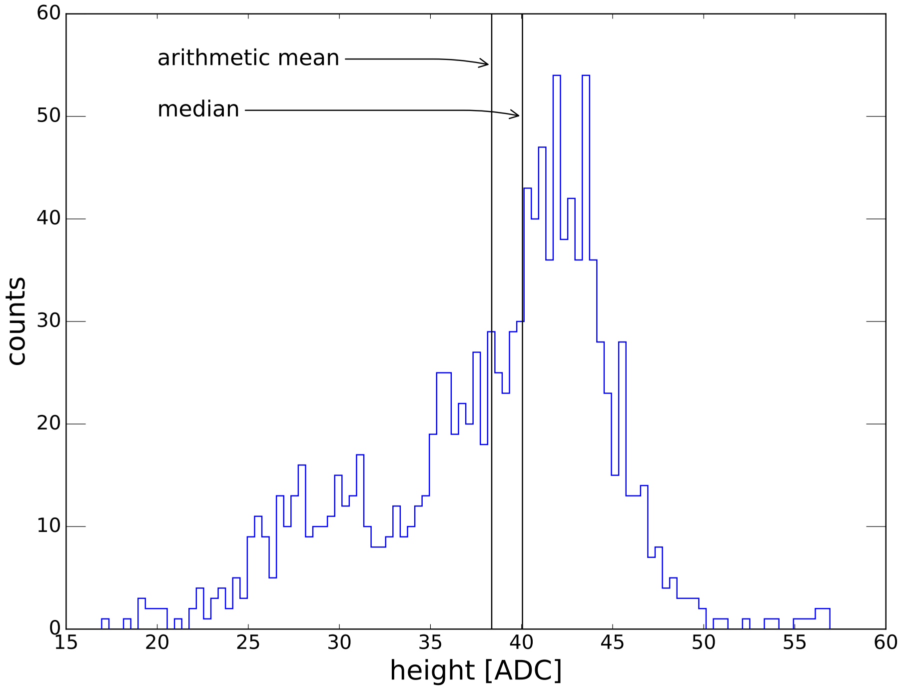

Figure 4.5.: Histogram of height of the slice marked in fig. 4.4 (0.5 pe to 0.55 pe) for channel 7.

4.1.3. Camparison to Fixed Window Integration Method

In [15], a method has been described for the PMT gain calibration. In order to compare the suggested technique above to this established method, the working principle should be briefly explained. Afterwards, the gains determined by both methods will be compared. For this calibration, the same data set as for the new method was used.
The fixed window method summarizes a fixed number of samples for each event and PMT. Empirically it has been found, that a window of 10 to 20 samples is practical. For most events and channels, there is no signal different from noise in this window. At the set voltage of 970 mV (see above for whole set of parameters), actual hits fall into this window in approximately 5% of all cases, which is desirable for good results. With less probability, two or more photo electrons are produced in this window. For all events and channels, the sums of samples are filled into a histogram. An exemplary histogram for channel 13 is shown in fig. 4.6.

The results are shown in table 4.3. In order to compare these gains with the ones obtained by the new method, the ratios of the gains and sigmas of the new to the old method are shown in table 4.4. Between both methods, a discrepancy of up to 113%(channel 6)

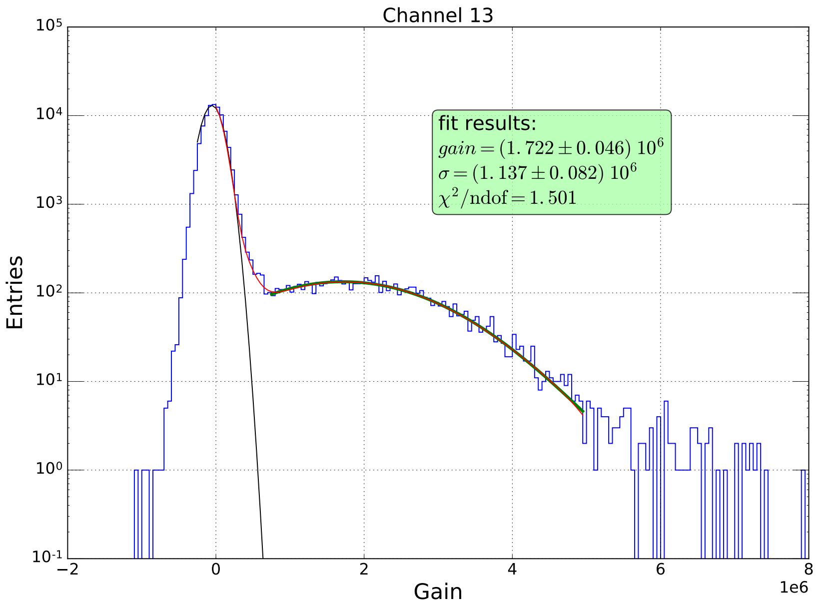

Figure 4.6.: Histogram of summed samples for channel 13.

can be seen. Nevertheless, for 8 of 14 PMTs the deviation amounts less than 25%. There is distinct trend towards higher gains but lower σ when using the new method. Only for channel 9 and 12 a lower gain was determined. A possible explanation could be that PAX is biasing the data by its working principle. As explained in section 4.1.1, PAX is looking for samples beyond the *high_threshold*. If low signals do not reach this threshold, they are ignored. The consequence is an apparently higher gain, as the lowest signals are cut off. The difference in the determined σs can be explained similarly. Fluctuations in the fixed window have a much higher effect than in the new method. The hit-finder primarily creates hits of 3 or fewer samples. Fluctuations are thus not as fatal as in the 10 or even 20 samples wide window.

The fixed window method should not bias the result in any preferred direction. However, its current implementation and the fitting of the histogram is not optimal yet, either. The size of the fixed window and the LED voltage can not be suitable for all PMTs, simultaneously. PMTs with comparatively low rates require a higher LED voltage in order to maintain the desired noise to signal ratio of 95% to 5%. However, with higher LED voltages the probability for multiple photon detections increases in brighter illuminated PMTs. In small boundaries, the size of the window can be adjusted accordingly. However, with bigger sizes of the windows the noise peaks' widths also increase.

Both methods have their advantages. Additional tests need to be done, in order to determine the right gain. It might be favorable to combine the methods in order to benefit from the advantages of both of them. A basic approach could be to let PAX find a certain number of hits per channel. With this number, the probability for a hit in a given number

Table 4.3.: Gains obtained by the fixed window method. A window of 10 samples was used. Fitting for Channel 4 did not converge. Error calculation for fit parameters of channel 5 failed.

Channel	Gain [10^6]	σ [10^5]
0	1.486 ± 0.094	0.992 ± 0.158
1	2.019 ± 0.259	1.578 ± 0.172
2	1.425 ± 0.056	1.375 ± 0.123
3	1.611 ± 0.053	2.110 ± 0.095
4	-	-
5	$0.634 \pm$ inf	$0.923 \pm$ inf
6	0.669 ± 0.080	0.951 ± 0.126
7	1.245 ± 0.082	0.963 ± 0.063
8	1.028 ± 0.090	0.905 ± 0.061
9	2.680 ± 0.279	1.520 ± 0.063
10	1.218 ± 0.100	1.355 ± 0.191
11	1.162 ± 0.042	0.870 ± 0.035
12	2.570 ± 1.282	2.261 ± 0.584
13	1.722 ± 0.046	1.137 ± 0.082

Table 4.4.: Ratio of gains and σ of new method to fixed window method

Channel	$\frac{\text{Gain}_{\text{new method}}}{\text{Gain}_{\text{fixed window method}}}$	$\frac{\sigma_{\text{new method}}}{\sigma_{\text{fixed window method}}}$
0	1.23	0.78
1	1.06	0.77
2	1.22	0.71
3	1.05	0.45
4	-	-
5	1.85	0.76
6	2.13	0.63
7	1.44	0.60
8	1.51	0.64
9	0.87	0.46
10	1.36	0.66
11	1.23	0.83
12	0.84	0.29
13	1.15	0.85

of samples can be estimated. In a second step, the fixed window width can be adapted according to this probability.

4.1.4. Problematic Channels

As shown in fig. 4.1, functionality was proven for all channels. However, channel 5 has a yet unknown source of noise. Unfortunately, this phenomenon does not cease in cold state. In the waveform shown in fig. 4.7, it can be seen that there is a sinus-like oscillation. In fig. 4.8 it is shown, that the waveform of a different event (taken from the same data set - about half a second later) has a complete different noise spectrum. In fact, further investigations with an oscilloscope showed that the frequencies of these oscillations go up to 300 MHz. Signals of these frequencies exceeds the sampling rate of 100 MHz by far and thus violates the Nyquist sampling theorem. As there is no single noise frequency, filtering this noise is a challenge. Thus, it is preferable to identify the reason for this high frequency noise first.
Nevertheless, the implications from this noise for channel 5 will lead to several problems. In fig. 4.7 it can be seen that a probably real single photo electron was not found, as the noise sets the threshold too high. In fig. 4.8, a different error is shown. Here, additionally to the possibly real single photo electron signal in the third hit, two other hits of noise were found. Furthermore, the width of these hits amounts to several hundred ns, which leads to more samples of noise being added to the hit.
In summary, the noise which is present in most of channel 5's waveforms leads to missing and falsely found hits. The gain calibration[3] for this channel has thus to be regarded with caution. Though there are noise-free waveforms for this channel, the amount of noisy waveforms can lead to unusable hits, peaks and events. Though it is hard to discard a partly working PMT completely, the channel should be turned off during acquisition, or in later analysis as long as there is no better solution.

[3]The gain calibration was used for figs. 4.7 to 4.8 for the right handed y-axis already.

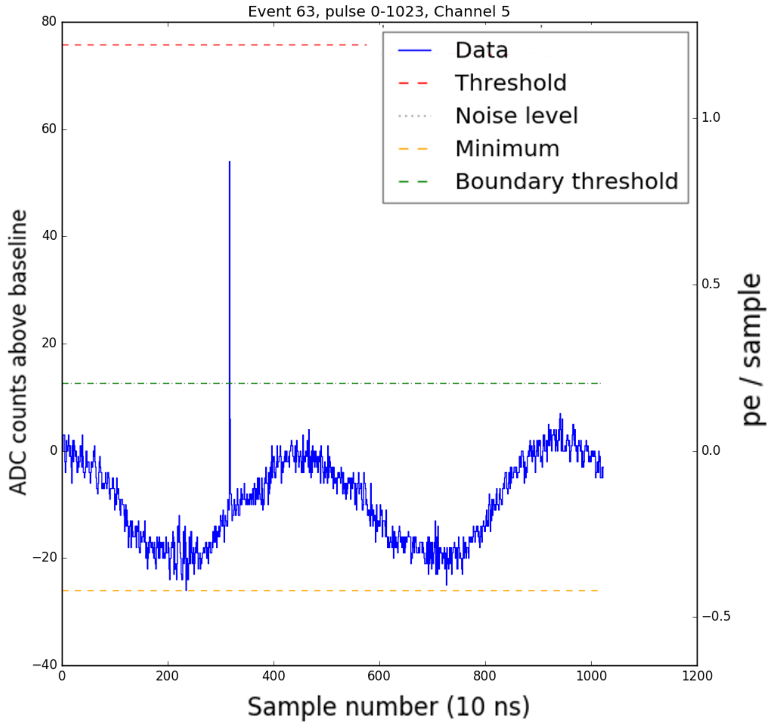

Figure 4.7.: Waveforms of event 63 in channel 5 in an LED calibration data set. Measurement has been performed at room temperature.

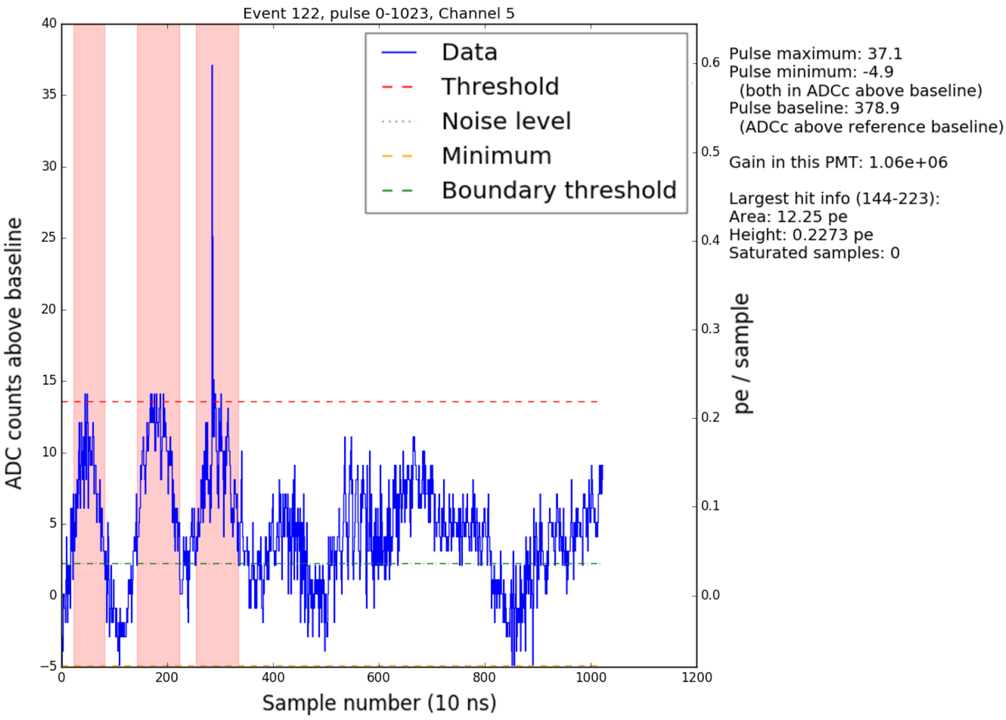

Figure 4.8.: Waveforms of event 122 in channel 5 in an LED calibration data set. Measurement has been performed at room temperature.

5. Kr83m Measurements in a Single Phase Gaseous TPC

Measurements have been performed with ^{83}Kr^{m} doped xenon in gaseous phase, without an electric field. ^{83}Kr^{m} is a metastable isotope produced in the β-decay of ^{83}Rb (see below). There are two main advantages, which make measurements in this mode of operation promising.
The first advantage is a more homogeneous distribution of the ^{83}Kr^{m} that can be assumed as the diffusion of krypton should be faster within a gaseous phase than in the liquid phase. Also, the circulation flow can be set to higher values as it is not limited by the lack of cooling power when having to liquify the xenon.
The second advantage is the lack of a transition surface between liquid and gaseous phase. In dual phase mode, this will cause - due to the large difference in index of refraction - a reflection of the scintillation light.

^{83}Kr^{m} is a practical choice for calibration as it has two distinguishable transitions (see fig. 5.1). It is produced in the beta decay of Rb83. The half-life of 1.83 h makes it possible

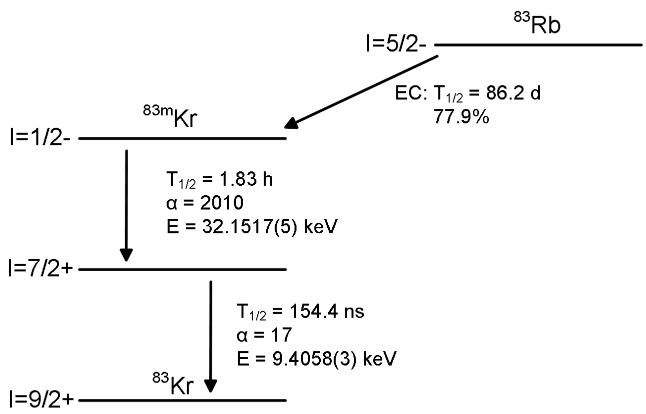

Figure 5.1.: Energy level diagram (in keV) for the ^{83}Rb decay. Each ^{83}Rb decays 77.9% of the time to the long-lived isomeric ^{83}Kr^{m} level 41.5 keV above the ground state, which subsequently decays in two steps, emitting a 32.1 keV and then a 9.4 keV conversion electron or a gamma. A direct decay from the ^{83}Kr^{m} to the ground state is suppressed. Figure from [17]

.

to take measurements without radioactively spoiling the TPC for more than a day.
One measurement was performed to observe the rise of the ^{83}Kr^{m} concentration, while

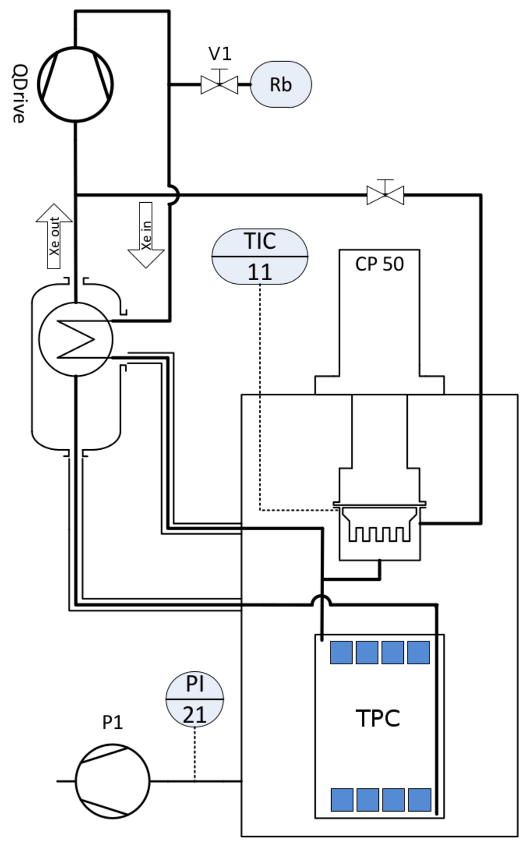

Figure 5.2.: Relevant components of fowchart of TPC, QDrive and Rb-source. The whole gas system is described in [17]. Image by C. Huhmann.

the valve V1 to the Rb83 source (see fig. 5.2) was opened. After a certain mixing time, an equilibrium between the production of $^{83}\mathrm{Kr}^{\mathrm{m}}$ and its decay should be reached. When then the valve is closed again, a decrease due to the decay of the $^{83}\mathrm{Kr}^{\mathrm{m}}$ would be expected. The measurement was performed in a warm state, while the circulation was set to 6 slpm. The time profile of the event rate can be seen in fig. 5.3.

The idle event rate amounts to about 12 Hz. Within two hours, the rate had risen to about 250 Hz. After about six hours, the event rate stabilized at approximately 350 Hz. 15.2 hours after the start of the measurement, the valve to the source was closed. First, the rate rose almost immediately by about 100 Hz, then the event rate dropped exponentially as would be expected due to the $^{83}\mathrm{Kr}^{\mathrm{m}}$ decay. The sudden increase of the rate could be a result from a "push-in" of $^{83}\mathrm{Kr}^{\mathrm{m}}$ enriched gas, when the valve was closed. The life-time of $\tau = (9518.3 \pm 13.5)$ s corresponds to a half-life of (1.83 ± 0.01) h. It matches the result that would be expected by [18]. The value was obtained from an exponential fit to the dark count rate corrected data and was done using the least squares method with the SciPy libraries[19]. The fit started at 56 000 s. To test the goodness of the fit, the value χ^2

was calculated by the following equation:

$$\chi^2 = \sum_i \left(\frac{n_i - \langle \text{baseline} \rangle - \exp\left(\frac{1}{\tau} \cdot t\right)}{\sqrt{n_i - \langle \text{baseline} \rangle + \text{stdv}\left(\langle \text{baseline} \rangle\right)}} \right)^2 \tag{5.1}$$

In eq. (5.1), n_i is the count rate for each second, $\langle$baseline$\rangle$ is the baseline obtained by averaging the first 600 s of the measurement (before V1 was opened) and stdv ($\langle$baseline$\rangle$) is the accordingly standard deviation.

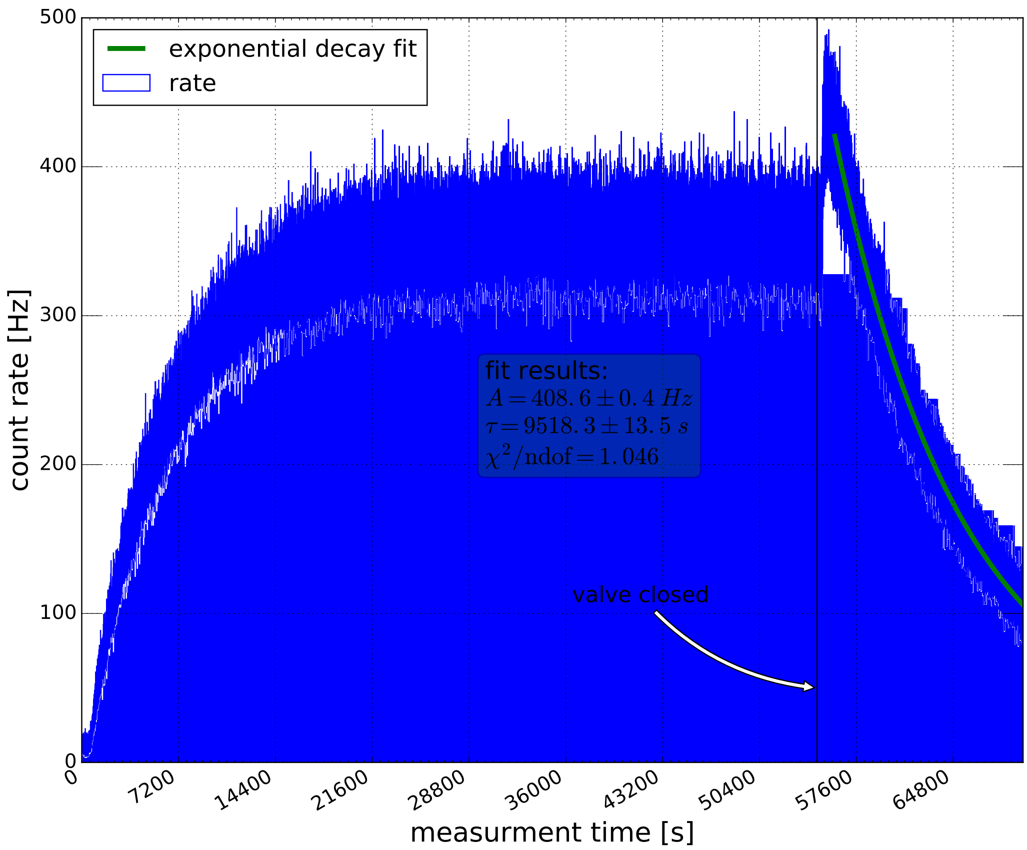

Figure 5.3.: Event rate over time. The parameters for the exponential are $A = (408.6 \pm 0.4)\,\text{s}^{-1}$, $\tau = (9518.3 \pm 13.5)\,\text{s}$.

6. Dual phase Measurement with a ^{137}Cs Source

After filling the TPC with liquid xenon, a measurement in dual-phase mode has been conducted. In order to do so, a ^{137}Cs source was used which had been placed outside of the insulating vessel. The filling was observed by three capacitive level meters, whose functionality and readout is described in [20]. For data acquisition, the zero-suppression threshold were set to 0.5 pe according to the method described in section 4.1.2. The triggering thresholds were only set for the top PMTs, as a triggering on the S2 signal is desirable. Also, the position of the trigger within the event was set to 800 samples from the end in the 8192 samples long event. Furthermore, high voltages of 10.72 kV and 2.78 kV were applied to the cathode and anode respectively. An event summary plot, which PAX is capable to produce, is shown in fig. 6.1. This sums up information about an exemplary event which contains an S2 and S1 signal.

It can be seen that there are several plots. The first two plots in the first row belong to the main S1/S2 interaction and show a zoom on the summed waveform of all channels, which is shown in the middle row plot. The last two plots of the first row show hit patterns for these peaks. For the S1 and the S2 signal, the hit pattern for the bottom PMTs and top PMTs are shown respectively. This is practical because the PMT-individual light collection efficiencies for the S1 signal are due to reflection at the surface in general better for the bottom PMTs. As the Münster TPC is rather small in diameter, most channels see hits. For larger TPCs like XENON100 or XENON1T, the approximate xy-position can already be guessed from the hit pattern for the S2 signal already. The bottom plot shows individual hits for each channel. Different sizes and colors represent different heights and areas of hits. Furthermore, "suspicious"[1] hits are marked in green. The gray underlay identifies where pulses were present in the event. An example for theses pulses can be found in channel 5 (due to high noise, see section 4.1.4), where there is a single pulse over the whole event with only few hits compared to other signals.
This plot shows that PAX is able to separate S1 and S2 signals for the Münster TPC. Future measurements will cover energy calibration. For that stable conditions of the TPC are crucial.

[1] PAX is able to identify suspicious channels. If a channel is producing too many signals or fulfills other criterea, suspicious hits are marked as such and ignored.

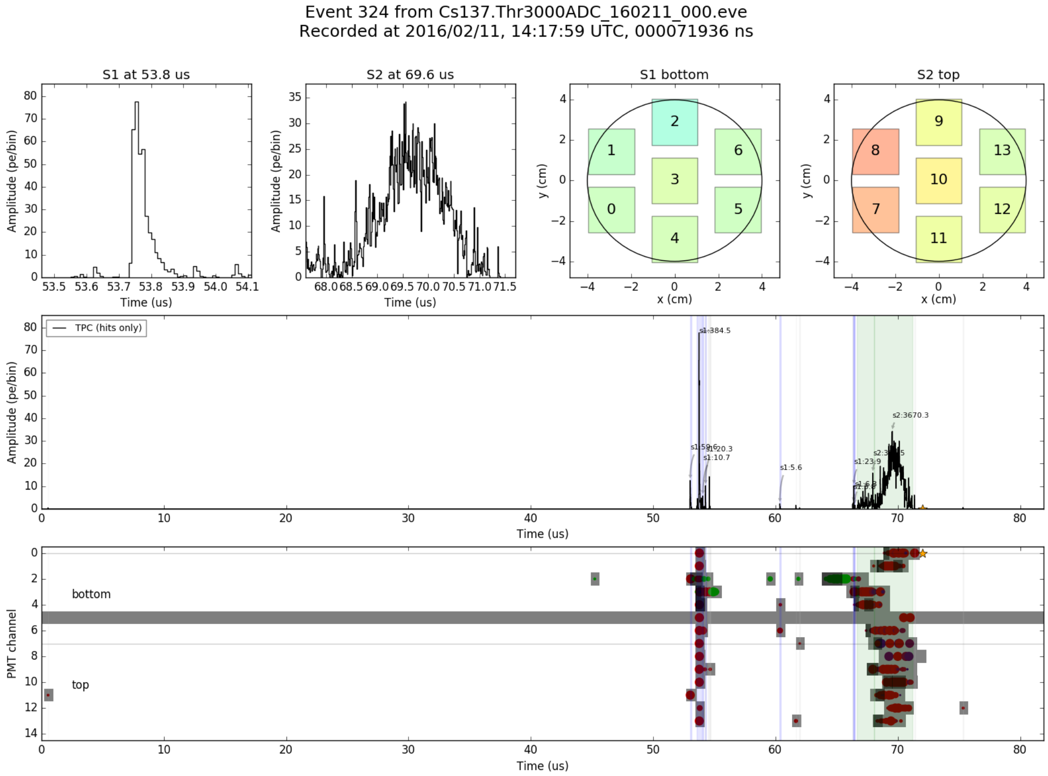

Figure 6.1.: Event summary plot of ^{137}Cs measurement.

7. A Magnetically Driven Piston Pump

For the gas circulation of high-purity experiments like XENON1T, a suitable pump is crucial. In order to keep the xenon gas in its high-purity state, it has to be continuously circulated through a purification system. Furthermore, the radon emanation, which is a property dependent on the used materials in all components, needs to be as low as possible. With a measured radioactivity of (11.9 ± 3.9) mBq[21], the currently used pumps have a higher activity than was expected beforehand.
The requirements concerning differential pressure and flow originate from the used components, as well as of the size of the gas system. For example, a differential pressure of at least 1 bar is needed for a proper operation of a getter. This device purges the gas from electronegative impurities which constantly accumulate in the system. Furthermore, a high flow is desirable, as these impurities would otherwise not be removed as fast as they appear.
For this reason, a new pump is being developed at Münster University in collaboration with Stanford University and the Rensselaer Polytechnic Institute. The design of a hermetically sealed, magnetically driven piston pump was adapted from a pump developed for the EXO-200 experiment [22]. The magnetic setup, which has been described in detail in [23] was developed in Münster in 2013. In the following, the proceedings of the setup are shown. This will contain the outer design, e.g. the motor and the frame. Also, a redesign of crucial parts whose performance turned out to be insufficient in their first version will be shown.

In a nutshell, the design of this pump is a reciprocating compressor, whose piston is moved by a magnetic field. This field is provided by a ring, which is then moved mechanically along the cylinder. Both ring and piston contain three individual magnetic rings with alternating polarity in axial direction (as shown among other things in fig. 7.8 and in [23]). The advantage of this magnetic orientation is a higher coupling strength in contrast with a radial orientation. The crucial advantage of this design altogether is the guaranteed purity of the gas even in the case of failure. Other types of pumps might contaminate the gas in the case of failure, possibly taking out the rest of the experiment.

In order to test the pump's properties and its performance in particular, a pump testing station (PTS) has been built in Münster. It is capable of measuring flow, inlet- and outlet pressure, as well as impurities of a connected pump [23]. A flowchart is shown in fig. 7.2 in the chapter of the gas line setup. Due to the high costs of xenon, all test were performed with argon.

Figure 7.1.: Photo of pump setup. Left: control rack with PC for sensor read-out and a frequency converter to control the motor. Middle: the magnetically driven piston pump. Lower right: pump testing station. The gas system has a total volume of approximately 32 l.

7.1. Outer Frame and Drive

In order to move the ring along the piston, an outer frame and motor are needed to mount the tube and to provide a low-friction drive. Tests and calculations in [23] indicated that in order to achieve a design value in differential pressure of 2 bar between the pump's in- and outlet, the magnetic coupling and thus the frame has to sustain a force of at least 2500 N . Furthermore, any torsion within the frame has to be limited to an absolute minimum as the ring has to slide along the cylinder without rubbing against it. For easy alignment an aluminum KANYA® frame was designed and built in Münster. The current setup is shown in fig. 7.1.

A vertical setup was chosen, as the self weight of the piston (≈6 kg) would result in a single-sided wear within the cylinder, along with other advantages like safety and easier accessibility. The only objection against this is that the gravitational force may cause unexpected long-term problems due to anisotropies between the up and down motion of the piston and ring. For the time being, the difference in force between the up and down cycle caused by the piston's self-weight may limit the available force for compression by less than 100 N. This should be negligible against the expected 2500 N.

In order to ensure a low friction motion along the tube, the ring is connected to a slide which is moving on rails which are mounted on the frame. By careful adjustment of these rails, a rubbing against the tube of ring could be removed completely.

The slide is connected to a conrod which is connected via a crankshaft to an AC motor (SEW KA67 DRE100LC/TF). This motor is controlled by a frequency converter (SEW MC07B0030-5A3-4-00) to allow operation at adjustable speeds. Furthermore, parameters such as frequency and current can be readout from the converter's display. As the nominal speed of the motor amounts to 1400 rpm, a gear unit with a transmission ratio of 59/1400 is needed. Thus, the maximum drive frequency on the pump's side amounts to almost 1 Hz.

7.2. Gas Line Setup

In fig. 7.2 a flow chart of the pump setup is shown. Within the pump, flapper valves (see section 7.3.2) allow only one-directional flow (FV 1-FV 4). In a single stroke (without loss of generality upwards), the gas in the volume above the piston gets compressed and eventually escapes through FV 3. Simultaneously, gas from the inlet side flows via FV 2 into the volume beneath the piston. Afterwards, the cycle repeats and gas flows in through FV 1 and out of FV 4. To observe the actual pressure on the top and bottom side of the piston, two pressure sensors are connected to the service ports on the respective sides(PI 02 and PI 01). They are needed to monitor the real pressure difference between both piston sides, as this is the value responsible for decoupling. In the following, the term *piston pressure* is used for this inner pressure difference, while the term *differential pressure* is used for the pressure difference measured at the pump testing station.
A relief valve is set to open at a differential pressure to prevent a decoupling between ring and piston if the force caused by the piston pressure exceeds the maximum coupling force of the magnets. However, it will not prevent decoupling by other reasons, e.g. friction of the piston. Furthermore, most valves (V 3, V 4, V 5 and V 6) are used during evacuation the pump through a dedicated KF flange (located behind V 6). During operation, they are usually shut. In order to provide a rather steady flow, two 12 L buffer volumes are located at the pump's outlet. Another buffer volume of approximately 4 L is built intos the PTS. The full volume of the setup was measured by integrating the flow through the flow controller FIC 01. It amounts to approximately 31.5 sl.

7.3. Leakage Measurements

In order to assure proper operation, two essential components need to seal the high from the low pressure side. Firstly, the piston gaskets which are responsible to seal the two volumes above and beneath the piston. Secondly, the flapper valves need allow only one-directional flow and inhibit leakage from the outlet towards the inlet.

7.3.1. Piston Gaskets

The only non-metallic component of the pump are the piston gaskets. They are made of UHMWPE[1] as it has the lowest friction property of the tested materials[22]. Furthermore, stability and reliability of these gaskets are crucial, for the purpose of keeping the piston at a precisely central position within the honed cylinder. In order to test whether the piston gaskets seal with an acceptable performance, the leakage rate was determined by measuring the flow around the piston. For that, the middle flanges (which contain the flappers) were dismounted and the VCR connection on one side of the pump was opened towards the atmosphere. On the other side, the argon bottle was attached with the PTS for pressure and flow measuring in between. The result is shown in fig. 7.3 The measurement showed a leakage rate of (185.85 ± 1.14) slpm/bar for the original set of gaskets. As

[1] ultra high molecular weight polyethylene

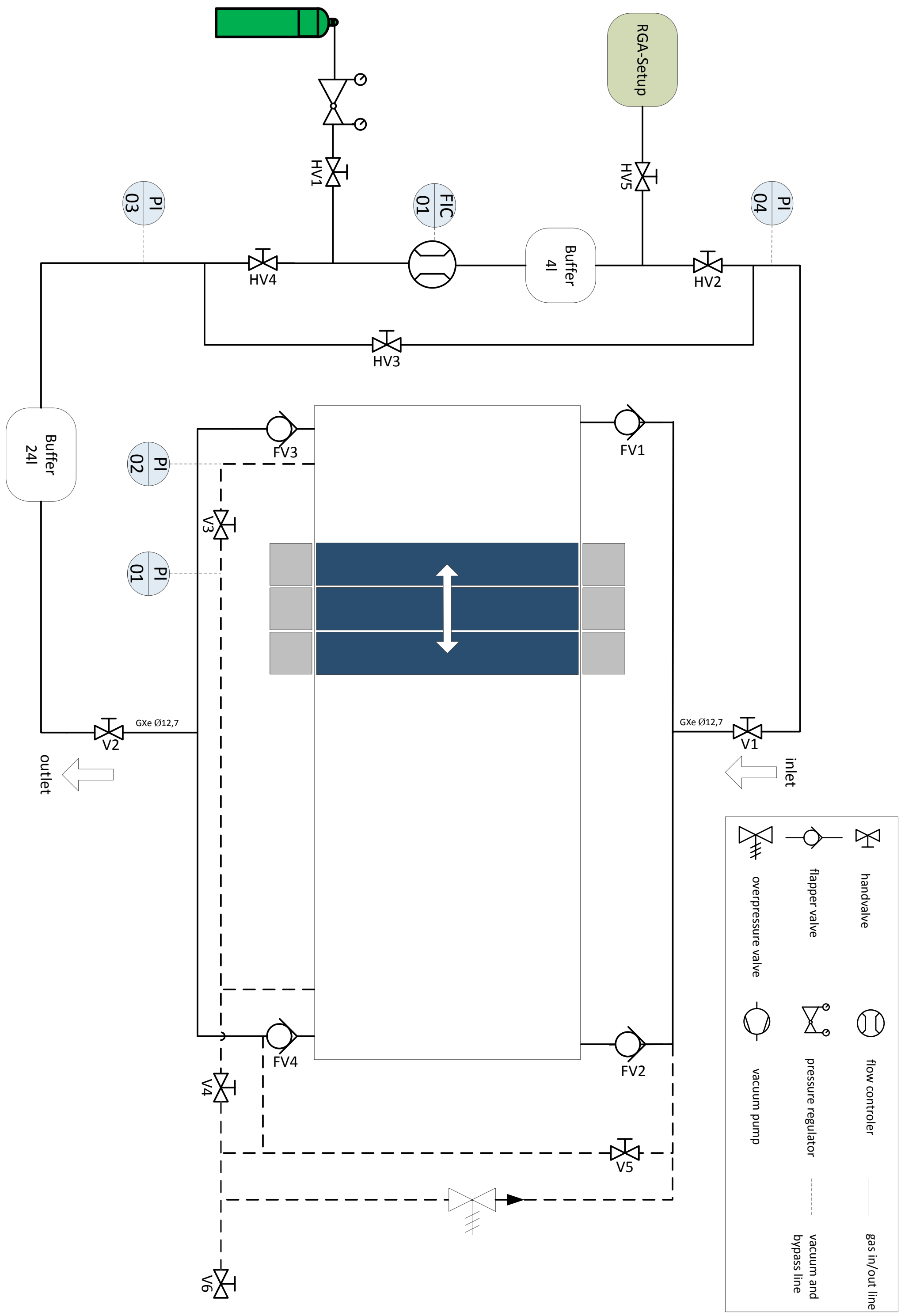

Figure 7.2.: Flowchart of pump connected to PTS. Right-hand-side: xenonpump. Left-hand-side PTS. Image by Christian Huhmann.

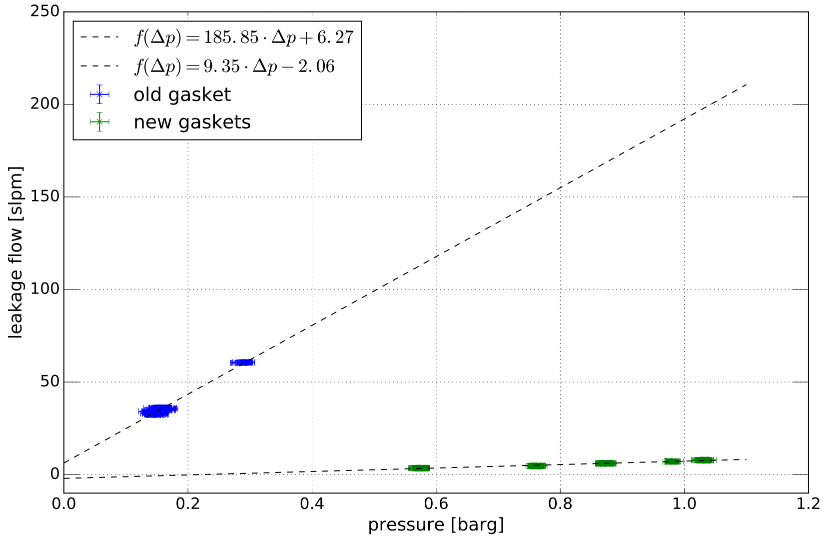

Figure 7.3.: Leakage flow versus differential pressure.

higher differential pressures could not be set due to the limited provision of argon by the bottle, higher values for the original set of gaskets can only be extrapolated linearly. However, this linearity is only given for laminar flow. At higher flows, when the formerly laminar flow eventually becomes turbulent, the flow would decrease relatively.
Also, one of the original gasket was vented through, as it was tried to be avoided to trap gas between the gaskets. However, as the leakage turned out to be too high for the desired performance, this problem was deferred and new double sealing gasket pair (see fig. 7.4) was designed and built. For the new pair of gaskets, a much lower leakage rate

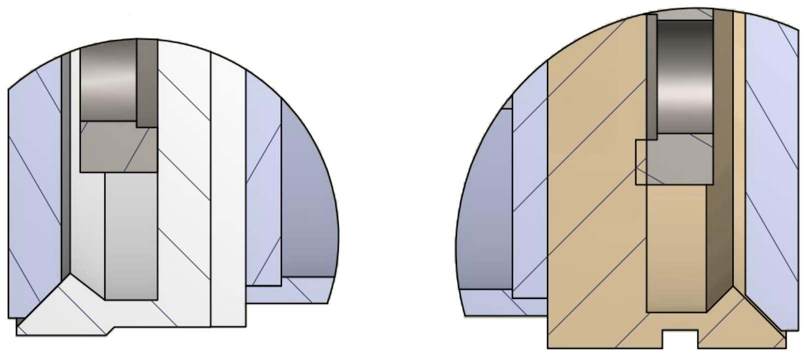

Figure 7.4.: Detail view of old and new gaskets. Left: old design with only 1 sealing surface. Right: new design with two sealing surfaces. See appendix for image of whole gasket in detail. Drawing by C. Huhmann.

of (9.38 ± 0.09) slpm/bar was measured. In this design, both gaskets are sealing and the pump was in vertical position, in contrast to the previous test which was performed still in horizontal position. Furthermore, the profile was varied to seal at the full distance. In the original version, only part of the gasket was sealing to the cylinder's wall as the design was adopted from the pump presented in [22].

It should be noticed that both tests were performed at a single position in the cylinder. Although the inner cylinder wall was honed, the leakage rate might differ along the stroke. So far, no obvious signs of inhomogeneities have been observed though.

7.3.2. Flapper redesign

To ensure only one-directional flow, flapper valves are installed in the inner flange of the pump (see fig. 7.2). A first set of flappers has been tested after less than an hour of pumping at moderate conditions (lower than presented in section 7.4.1). As can be seen

Figure 7.5.: Old flapper after less than an hour of operation. The plastic deformation leads to higher leakage.

in fig. 7.5, the flappers got damaged as they were sucked into the hole which they are supposed to seal. In the long term, a further damage and thus fewer sealing properties can be expected. Furthermore, they might tear off at some point, possibly damaging the inner tube and piston gaskets.
Therefore, a new revision of flappers have been designed and built for safer operation and better sealing properties, which is shown in fig. 7.6. The new design used higher cross-sectional area holes (28 mm in diameter), which required an additional grid to prevent a soak in. Also, the flapper material was changed from stainless steel to spring steel with a thickness of 0.3 mm. The increased length of the flapper reduces the necessary tension at the fastening point. A mechanic constrain prevents the flapper from bending beyond its yield strength.

In order to test if the sealing properties of the new flappers improved, the pump was

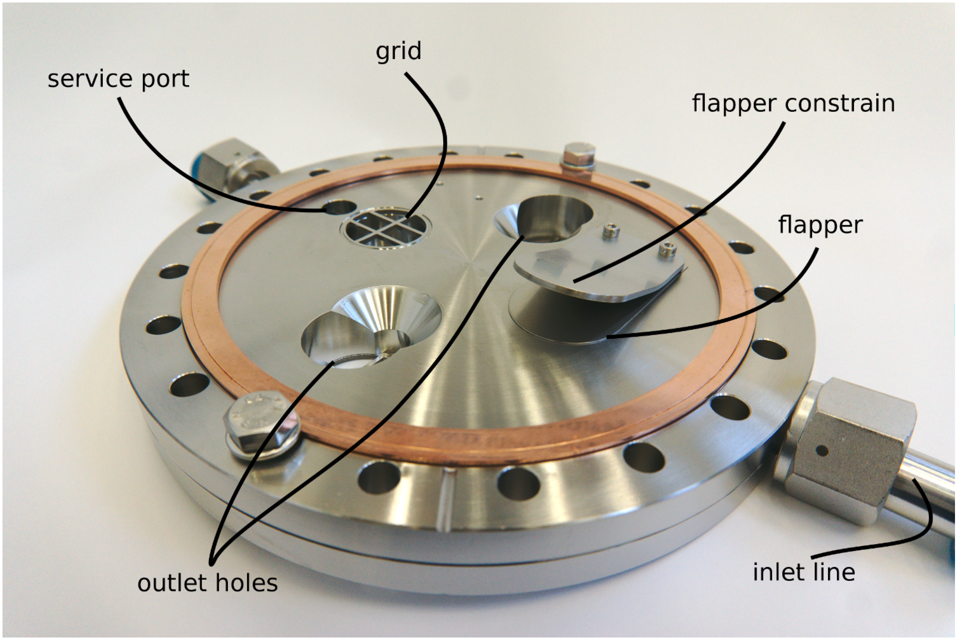

Figure 7.6.: New flapper design on the inner flange. Here, the inner side of the flange is shown. In front, one of the flapper has been installed already, while in the back, a grid which prevents a soak in is yet visible. From the other side, the outlet holes will be covered with another pair of flappers.

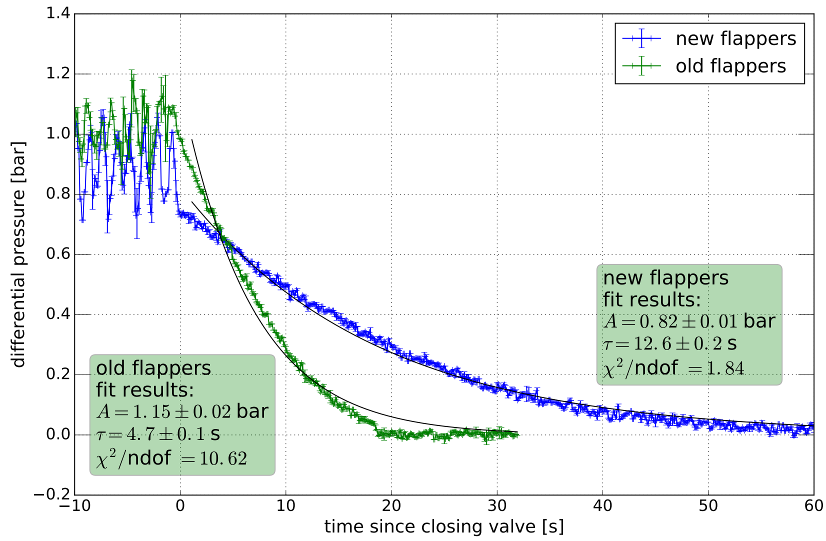

Figure 7.7.: Differential pressure after pump shutdown and simultaneous closing of V4.

turned off during operation at the bottom dead center, closing V4 at the PTS simultaneously. The only way for the gas on the outlet side to reach pressure equilibrium with the inlet side, is through the flappers in wrong direction. The time needed to reach equilibrium ($p_{\text{out}} - p_{\text{in}} = 0$) is a measure for leak-tightness. This can be seen in fig. 7.7. As the form of the differential pressure suggests, an exponential decrease can be fitted to the data. With that, a "lifetime" for the differential pressure can be specified. It is the time when the differential drops to its e^{-1}-fraction. For the old flappers this time amounts to $\tau = (4.7 \pm 0.1)$ s. The new flappers feature a τ of (12.6 ± 0.2) s. Though the new flappers have larger holes to seal, the ability to prevent wrong directional flow has been improved. This can most likely be explained by the damage of the old flappers.
The new flappers will still need to prove their reliability, as only few tests have been performed yet. However, after one hour of pumping at moderate conditions (see section 7.4.2) and a few shorter runs at higher speeds, the pump was opened and no signs of use could be seen.

7.4. Calculation of XENON pump performance

The amount of gas that is capable to bypass the piston gasket needs to be as low as possible. If this bypass flow was too high, hardly any differential pressure could be built up at a given speed of the piston. In this chapter, the maximal achievable differential pressure (or rather piston pressure) is calculated, which means pumping against a dead end. Limitations due to the magnetic coupling are not taken into account.

$$
\begin{aligned}
p_d(t) = p_c(t) - p_{\text{in}} &= \text{piston pressure} \\
p_{\text{in}} &= \text{absolute inlet pressure} \\
p_c(t) &= \text{absolute pressure on pump's outlet side} \\
p_{\text{out}} &= \text{constant pressure of gas system at pump's outlet side} \\
A &= \text{tube cross-sectional area} \\
x(t) &= \text{position of piston} \\
h &= \text{stroke length} \\
l &= \text{conrod length} \\
r &= \text{crankshaft length} \\
V_0 &= \text{estimated full volume in pump} \\
V_c(x(t)) = V_0 - A \cdot x(t) &= \text{currently compressed volume} \\
Q'_l &= \text{leakage rate per differential pressure} \\
Q_l = Q'_l \cdot p_d &= \text{leakage rate} \\
\alpha &= \text{angle with respect to the top dead center}
\end{aligned}
$$

V_0 was estimated from the CAD-drawing, using the actual crankshaft length which was used for the following tests. The motion of the piston can be described with:

$$x(t) = \sqrt{l^2 - (r \cdot \sin\alpha)^2} - (r \cdot \cos\alpha) - (l - r) \tag{7.1}$$

It can be estimated by the following equation:

$$x(t) = r \cdot (1 - \cos\alpha) \tag{7.2}$$

This is possible as the conrod is large compared to the radius of the motor's crankshaft. The difference between described motion in eq. (7.1) and eq. (7.2)is shown in fig. 7.9.

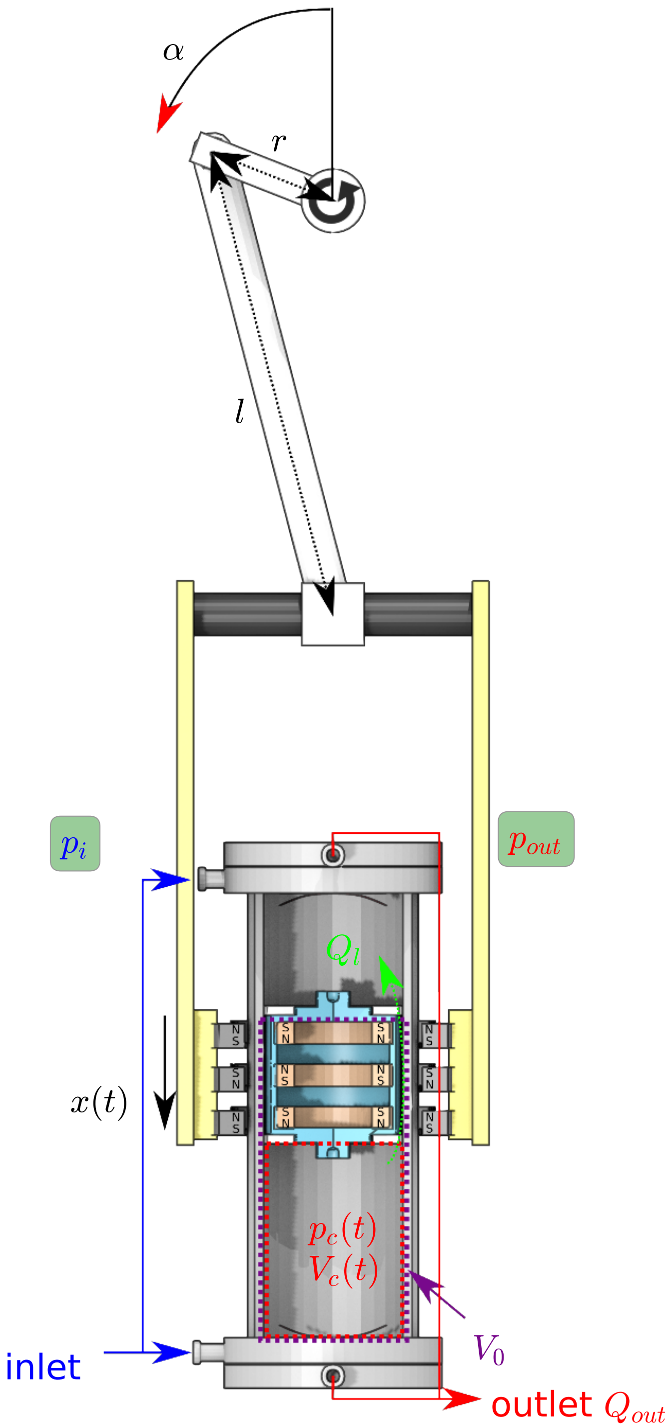

Figure 7.8.: Sketch of pump. Dimensions not to scale. The crankshaft and conrod are rotated by 90° to fit in the picture's plane.

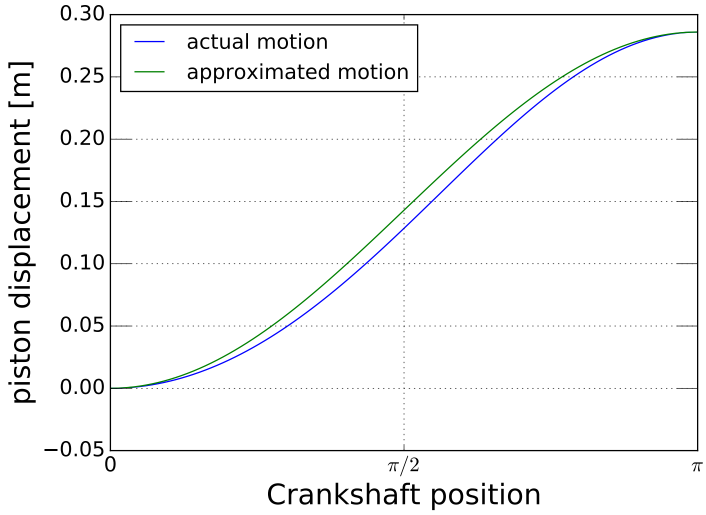

Figure 7.9.: Motion of piston vs approximated function

The output pressure is given by the compressed volume.

$$p_c(t) = p_{\text{in}} \cdot \frac{V_0}{V_c(t)} \tag{7.3}$$

In this term, an isothermal process is estimated. An adiabatic compression and thus a heating up during operation would result in a faster pressure increase. This effect is neglected here for now.

However, as the piston gaskets are not leak-tight, an additional term has to be added to factor in the flow which decreases the amount of compressed gas. This leakage increases with the differential pressure. Due to more turbulent flow at higher flow rates, it should decrease relatively with higher differential pressure. For reasons of simplicity - and because this effect did not occur up to 1 bar, see fig. 7.3 - it is considered to scale linearly in the following calculations.

$$Q_l = p_d(t) \cdot Q'_l \qquad Q'_l = \text{const.} \tag{7.4}$$

That leads to

$$p_d(t) = p_c(t) - p_{\text{in}} - \int_0^t \frac{Q_l t}{V_c} \text{dt} \tag{7.5}$$

$$= p_{\text{in}} \left(\frac{V_0}{V_c(t)} - 1 \right) - \int_0^t \frac{Q_l \cdot t}{V_c(t)} \text{dt} \tag{7.6}$$

Here, the assumption was made that on the not compressing side of the piston, enough gas flows in, so that the pressure stays constant at p_{in}. Substituting Q_l according to eq. (7.4), the expression becomes:

$$p_d(t) = p_{\text{in}}\left(\frac{V_0}{V_c}-1\right) - \frac{Q_l'}{V_c}\int_0^t p_d(t')dt \tag{7.7}$$

Here, the first term originates from the isothermal compression. The second term describes the loss of gas due to leakage around the piston. After rearranging, the formula can be differentiated :

$$\int_0^t p_d(t')dt' = -\frac{V_c p_{\text{in}}}{Q_l'} - \frac{V_c}{Q_l'} p_d(t) + \frac{V_0 p_{\text{in}}}{Q_l'} \tag{7.8}$$

$$p_d(t) - p_d(0) = -\frac{p_{\text{in}}}{Q_l'}\dot{V}_c - \frac{1}{Q_l'}\left(\dot{V}_c p_d(t) + V_c \dot{p}_d\right) \tag{7.9}$$

$p_d(0) = 0$ as there is no initial compression.

$$p_d(t) = -\frac{p_{\text{in}}}{Q_l'}\dot{V}_c - \frac{\dot{V}_c}{Q_l'} p_d(t) + \frac{V_c}{Q_l'}\dot{p}_d(t)$$

This inhomogeneous differential equation can be rearranged to

$$\dot{p}_d(t) \underbrace{- \frac{Q_l'}{V_c(t)}\left(1+\frac{\dot{V}_c(t)}{Q_l'}\right)}_{a(t)} p_d(t) = \underbrace{p_{\text{in}}\frac{\dot{V}_c(t)}{V_c(t)}}_{f(t)} \tag{7.10}$$

This equals the form of an inhomogeneous differential equation described in [24] :

$$\dot{u}(t) + a(t)u(t) = f(t) \tag{7.11}$$

that has the general solution:

$$u(t) = e^{-\int_{t_0}^t a(\zeta)d\zeta}\cdot\left[\int_{t_0}^t f(\zeta)\cdot e^{+\int_{t_0}^{\zeta} a(\eta)d\eta} d\zeta\right] \tag{7.12}$$

For this case $t_0 = 0$ and t goes up to the time for a full stroke $t_{\text{max}} = \frac{1}{2\pi\cdot\text{frequency}}$. There is no analytical solution for this integral, though. In the following, an iterative approach will be pursued.

Iterative solution The analytical solution ends up in a difficult and only numerical solvable equation (eq. (7.12)). A simpler approach is to use an iterative algorithm, that uses the first (and solvable) term from eq. (7.6) and take it as an approximation for $p_d(t)$ in the second term. This solution is then used for the next order, successively converging to the final solution. This series can be written as:

$$p_{d,i+1} = p_c(t) - p_{\text{in}} - \frac{1}{V_c(t)}\int_0^t Q_l' p_{d,i}(t')\mathrm{d}t' \tag{7.13}$$

As shown in fig. 7.10, the algorithm converges to a stable solution after single iteration for the given leakage of $Q_l' = 9.35\,\mathrm{sl/(bar \cdot min)}$. Moreover, it can be seen, that the desired pressure of 2 bar is reached after approximately 0.8 s at the frequency $f = 0.4\,\mathrm{Hz}$. After that, it increases to more than 6 bar. The leakage rate is based on the measurement of the new pair of gaskets(see section 7.3.1).

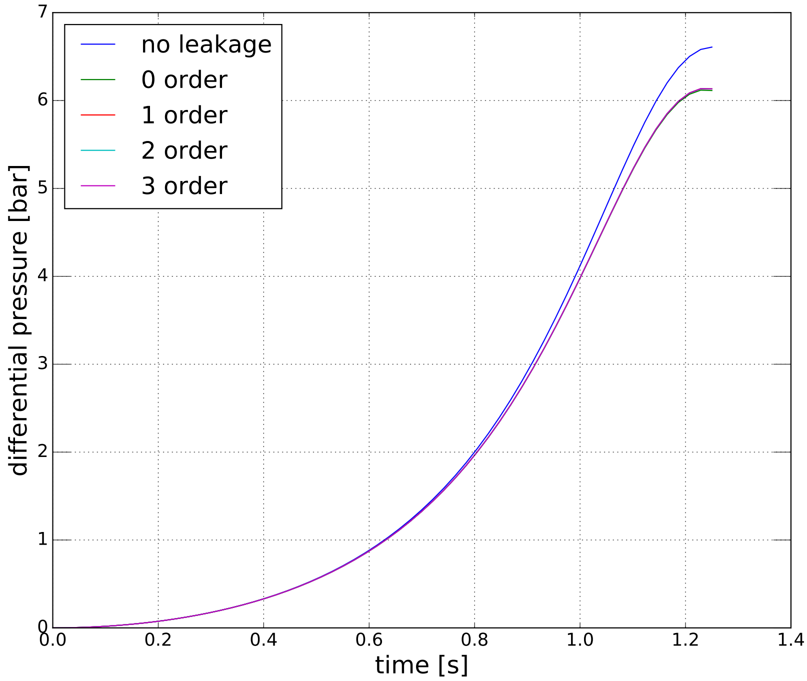

Figure 7.10.: Calculated differential pressure during a stroke at 0.4 Hz and an estimated leakage of $Q_l' = 9.35\,\mathrm{sl/(bar \cdot min)}$. The inlet pressure p_{in} amounts 1.4 bar.

The flattening in the slope of the pressure at the end of the stroke can be explained by the cosine-like motion (eq. (7.2)) of the piston. For higher leakages, the volume displacement of the piston becomes lower than the leakage rate at the current differential pressure.

Until the output pressure does not reach the value on the pump's outlet side p_{out}, the gas will stay in the compressed volume. Once it exceeds this counter-pressure, the pump will start pumping the gas out of the cylinder. At this point, only part of the stroke is yet available.

The flow that can be calculated from the following continuity equation:

$$V_c(t) \cdot p_c(t) + \int Q_{\mathrm{out}} \mathrm{d}t + \int Q_l' p_d(t) \mathrm{d}t = \mathrm{const.} \tag{7.14}$$

The constant is known, as both Q_{out} and the leakage term are zero for $t = 0$, leaving $V_c(0) \cdot p_c(0)$ which is:

$$V_c(0) \cdot p_c(0) = \text{const.} = p_{\text{in}} V_0 \tag{7.15}$$

Only if the output pressure prevails the constant pressure on the outlet side, gas can flow. Therefore, Q_{out} is zero until $p_c(t)$ exceeds p_{out}. Furthermore, $p_c(t)$ is in this simplification not increasing beyond p_{out}. Instead, the pressure opens the flapper valve and gas streams out of the pump. Thus, $p_c(t)$ and with that $p_d(t)$ stay constant. $p'_d(t)$ is a tuned function of eq. (7.6). It is defined as:

$$p'_d(t) = \min(p_d(t), p_{\text{out}} - p_{\text{in}}) \tag{7.16}$$

With these constrains, eq. (7.14) transforms to:

$$\int_0^t Q_{\text{out}} \mathrm{dt} = \begin{cases} 0 & \text{for } p_c(t) < p_{\text{out}} \\ p_{\text{in}} V_0 - Q'_l \int_0^{t_{\text{crit}}} p_d(t) \mathrm{dt} - p_{\text{out}} \cdot V_c(t) - Q'_l \cdot (p_{\text{out}} - p_{\text{in}})(t - t_{\text{crit}}) & \text{for } p_c(t) > p_{\text{out}} \end{cases} \tag{7.17}$$

Here, t_{crit} is the point in time at which the pressure is high enough to open the flapper valve.

The result for the same parameters as above and a p_{out} of 2.2 bar is shown in fig. 7.11. As already seen for the differential pressure(see fig. 7.10), the slower volume displacement leads to a flattening in the flowed gas at the end of the stroke. The total gas that has flowed at the end of the stroke amounts ≈ 4.23 sl. By derivating this curve, the flow can be calculated which is shown in the bottom of fig. 7.11. At this point, almost half of the stroke already passed. When the flapper valve opens, the flow out of the pump follows the same form as the piston's volume displacement. It peaks at 9.61 sl/s. This corresponds to 576.6 slpm.

From the calculated flow for a single stroke, a pumping performance of 206 slpm can be evaluated. The parameters have been chosen to match the conditions of a performance test which is presented in the next section.

7.4.1. Performance Measurements

In order to measure the performance of a pump, the previously mentioned pump testing station (PTS) was used. The setup's flowchart is shown in fig. 7.2. It is a closed system with a volume of approximately 31.5 L.

By measuring the flow - and the pressure between the pump's in- and outlet respectively - the performance can be analyzed. When the pump is turned on, valves V4 and V2 are completely open, while V 1, V 3, V 8, and V5 are closed. In this state, a differential pressure already establishes, depending on the current speed of the motor. The respective idle flow is due to the lack of any artificial resistance maximal. If then V4 is closed a bit at a time, the gas damns in front of it increasing the pressure at PI 02. At the same time, the flow measured by FI 01 decreases. This can be seen in fig. 7.12. The data was taken at

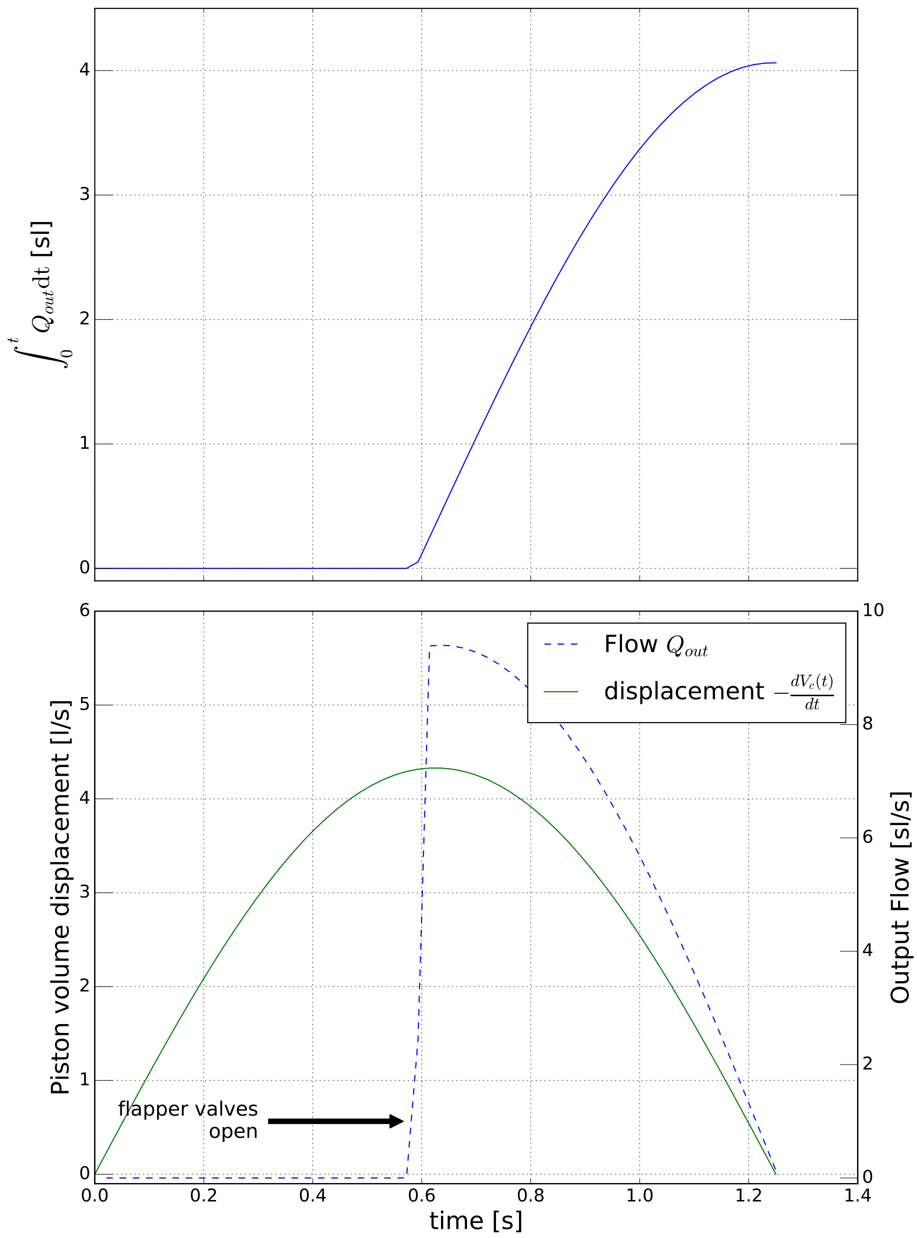

Figure 7.11.: Top: Gas flowed during one stroke at 0.4 Hz. Bottom: Derivative of upper plot and piston displacement.Leakage rate amounts to 9.35 sl/(bar · min).

a motor frequency of 550rpm. This corresponds to a frequency on the crankshaft's side of $f = 0.40\,\mathrm{Hz}$. Also, all values are oscillating with the frequency of the piston velocity, as the dampening effect of the buffer volumes cannot annihilate the entire stroke-like motion. The amplitude amounts to approximately 0.1 bar for the inlet pressure and a

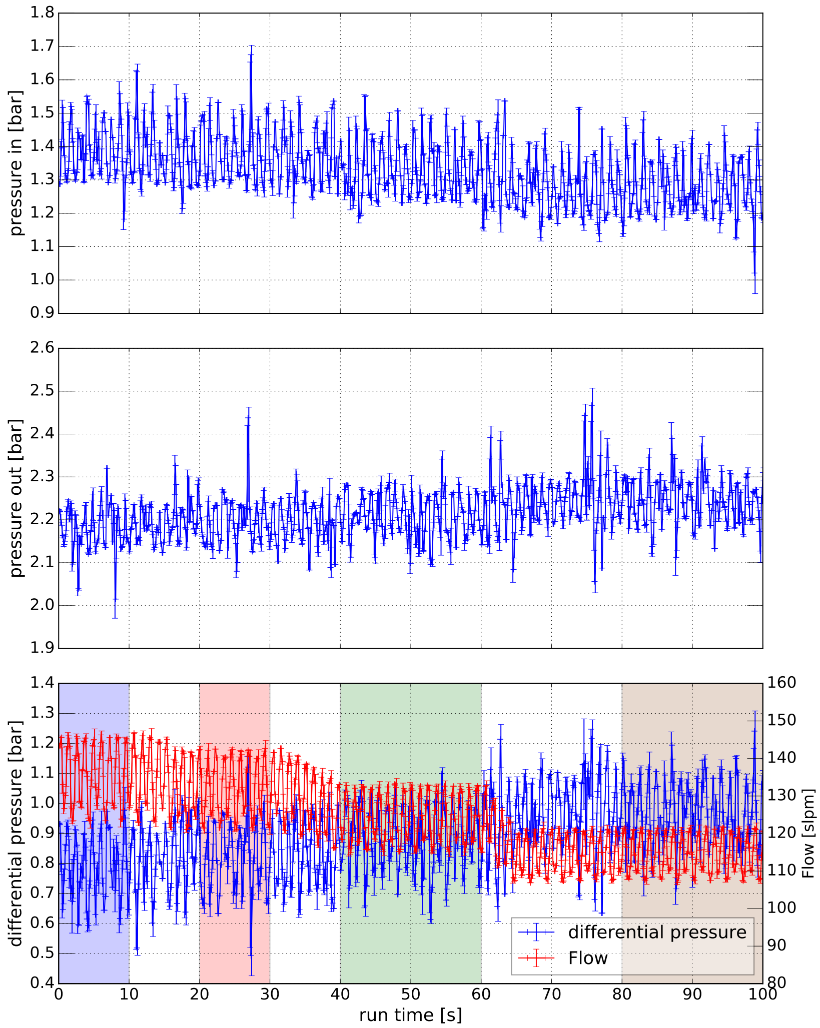

Figure 7.12.: Plot of inlet-, outlet-, differential pressure, and flow versus time. Gradually V4 at the PTS is closed up to 3/4 of a turn. Colored sections in the lowest plot will be used for performance determination shown in fig. 7.13

little less for the outlet pressure. It should be pointed out, that the differential pressure already oscillates in the idle state around 0.8 bar, with an amplitude of about 0.15 bar. The respective flow amounts to 120 slpm to 140 slpm. The fluctuation within the flow decreases to higher differential pressures as the buffer volumes holds the gas, therefore providing a steadier flow.

A performance specification to the above measurement can be generated by plotting the flow versus the differential pressure. This is shown in fig. 7.13. The data points (circle markers) indicated in the regions seen in fig. 7.12 create ellipses, which can be fitted by using the least squares method by [25]. This way, the centers can be determined and with these, the performance at yet unreachable differential pressures can be extrapolated. In this plot the piston pressure is also shown. This is the limiting factor for measuring at higher differential pressures as it would directly lead to a decoupling between piston and ring, when the pressure difference becomes greater than the maximum coupling force. With the current magnetic configuration, a piston pressure beyond 1.5 bar is unattainable.

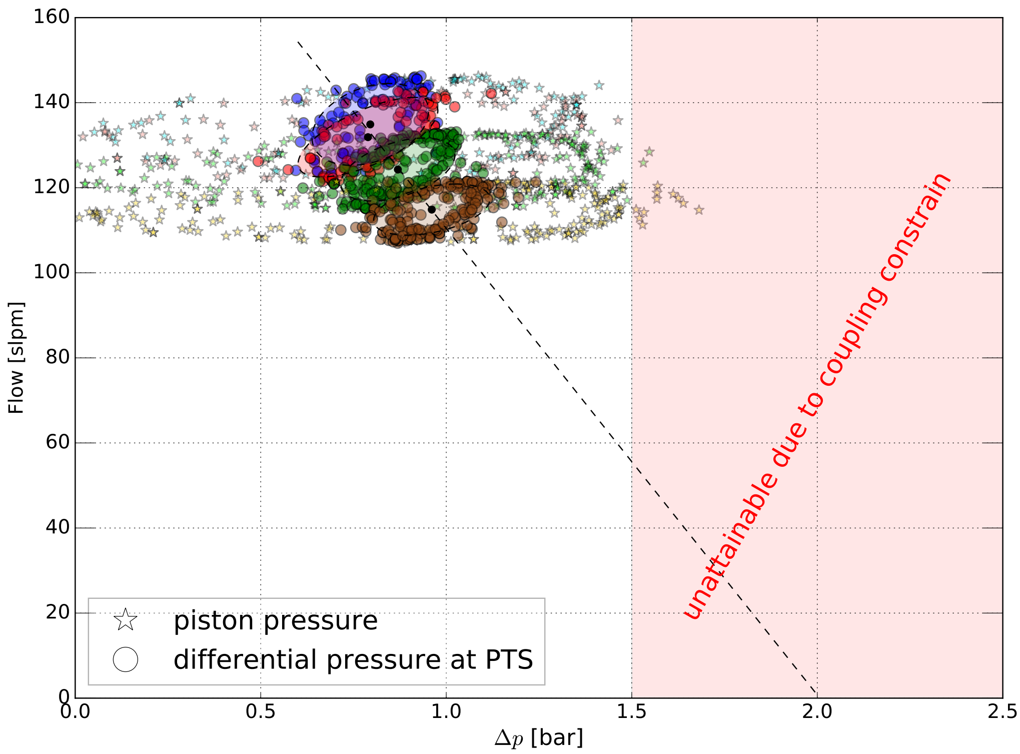

Figure 7.13.: Plot of flow versus differential pressure. Different colors correspond to the marked region in fig. 7.12.

In order to compare these values with the calculations, the measured parameters p_{in} and p_{out} have been used to calculate the respective flows. For the four different measurement points, the measured parameters and the flows calculated accordingly are shown in table 7.1. Furthermore, the efficiency is specified by the fraction of measured flow by the calculated flow. The efficiency amounts to 70% for the first measurement point and

Table 7.1.: Efficiency for the for different measurements

Measurement Point	p_{out}	p_{in}	$p_{\text{out}} - p_{\text{in}}$	Flow	Calculated Flow	Efficiency
0	1.39	2.18	0.79	135.62	193.38	0.70
1	1.38	2.20	0.82	132.19	191.28	0.69
2	1.33	2.21	0.88	124.31	180.22	0.69
3	1.28	2.24	0.97	114.54	167.02	0.69

69% for the other measurement points. As the range of differential pressures is rather small, it is not worthwhile to extrapolate towards higher differential pressures. There are some effects that did not go into the calculation, which reduce the efficiency. For example it was assumed, that the gas leaves the pump completely without any increase of pressure beyond p_{out} and that the displacement is reduced by the force on the piston. Moreover, whether the isothermal calculation describes the pump's pumping cycle sufficiently enough or another term for the adiabatic process needs to be added is questionable.

7.4.2. Long Term Test

It has been shown, that the pump is capable of providing a decent performance with respect to the limited coupling force. However, these tests did not take more than a couple of minutes before the pump had been turned off again. In order to test, whether the pump is capable of pumping for several hours without interruption, it was turned on at 420 rpm (motor side), which amounts to 0.3 Hz at piston side. Thus, the speed was reduced by 25% compared to the performance test described in section 7.4.1. Furthermore, the valves at the PTS were opened completely, hence reducing the load to a minimum. The pressure in the system amounted to 2.0 bar. The temporal development of the pump's sensors is shown in fig. 7.14.

It can be seen that the pressure and flow are rather stable for the whole test. However, there is a slight increase in the inlet and outlet pressure that can be explained by the gas warming up. The differential pressure stays constant, though. This even accounts for the beginning and the end of the test. In the regions approximately three minutes after the beginning and three minutes before the power off of the pump the flow is about 5 slpm to 10 slpm lower than in between. Seven minutes before the end of the operation - two minutes before the drop in the flow began - a "whistling" sound appeared when the ring was at the top dead center. With time, the volume increased slightly before a sudden sound indicated a decoupling between piston and ring. The pump needed to be manually turned off immediately. Before this will be investigated further, the temporal behavior of the temperature should be dealt with.

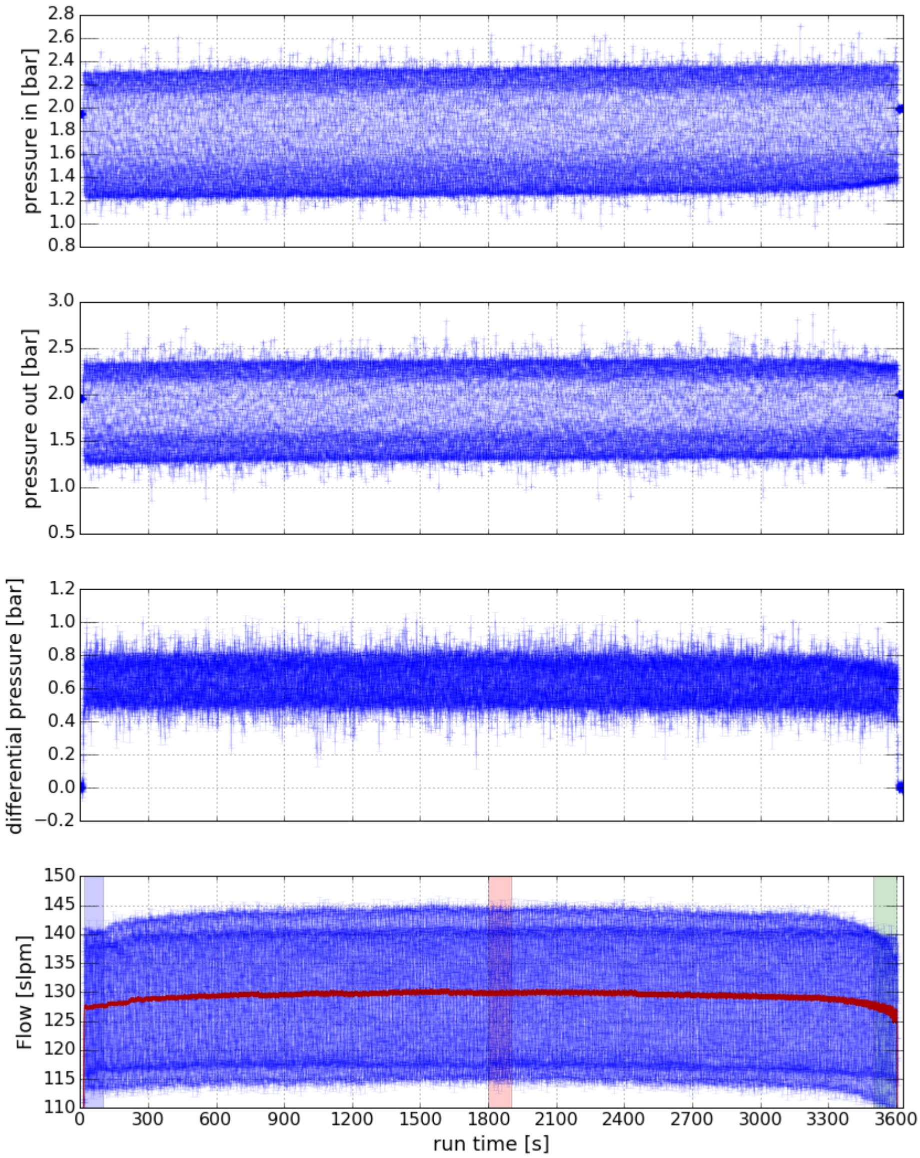

Figure 7.14.: Temporal development of sensors versus time. The test ended with a decoupling of the piston and a prompt emergency power off. For better visibility, a 3 s average of the flow is overlayed bottom plot. Furthermore, three regions are marked which are used in fig. 7.16.

In order to measure the temperature evolution during operation, four (PT 100 and PT 1000) sensors (which can also be seen in fig. 7.1) have been attached to the testing setup. They are mounted at:

1. the top outlet line (PT 100),
2. the join of both outlet lines (PT 1000),
3. the join of inlet lines (PT 100), and
4. the tube below the lowest position of the ring during operation (PT 1000).

The temporal development of the temperatures is shown in fig. 7.15. It is shown, that all sensors are rising with time. However, the temperature of the inlet sensor only increases by 1 °C during the whole measurement, whereas both outlet sensor values increase by approximately 13 °C within the first ten minutes. After that, they increase indefinitely with a decreased slope, until the pump was turned off. The middle of the tube even felt a couple of minutes after the power off hotter than the temperature at the outlet top (estimate 50 °C). With the nearby flange and the distance towards the rubbing gaskets, the tube bottom sensor does not give accurate results for the tube's temperature in the relevant region. An upper boundary for the temperature increase by compression can be calculated by thermodynamics's laws of adiabatic compression:

$$p_{\text{in}} V_0^{\kappa} = p_c(t) V_c(t)^{\kappa} = \text{const.} \qquad \text{and} \tag{7.18}$$

$$T_{\text{in}} V_0^{\kappa} = T_c(t) V_c(t)^{\kappa} = \text{const.} \tag{7.19}$$

Here, κ is the adiabatic index[2], T_{in} and $T_c(t)$ are the temperatures of incoming gas and the compressed gas respectively. From these formulas follows:

$$T_c(t) = T_{\text{in}} \left(\frac{p_c(t)}{p_{\text{in}}} \right)^{\frac{\kappa-1}{\kappa}} \tag{7.20}$$

For $T_{\text{in}} = 21\,°\text{C}$ (294 K), $p_{\text{in}} = 1.4\,\text{bar}$, $p_c(t) = 2.4\,\text{bar}$ (using p_{bottom} and p_{top}) and an adiabatic index of 1.67 [26], a temperature of 92 °C can be expected. As any heat transfer is neglected here, this value can only be an upper limit.

[2] The adiabatic index is often also referred to as the specific-heat ratio

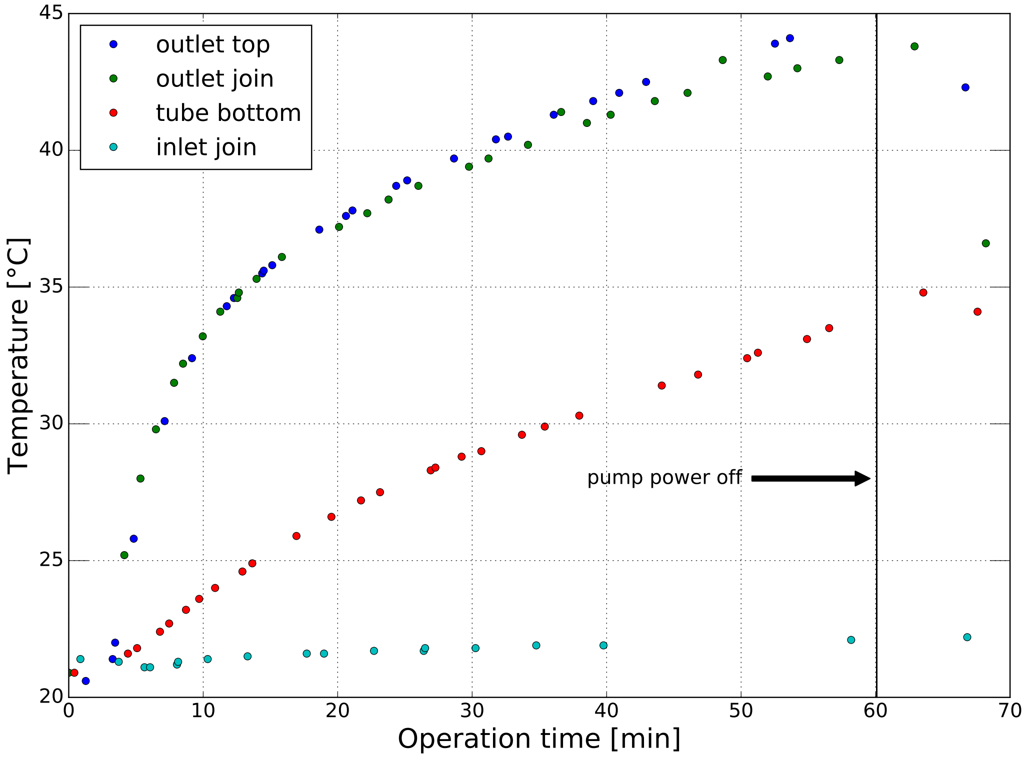

Figure 7.15.: Temperature evolution of selected parts of the pump

Investigation of anisotropies As shown in fig. 7.14, the flow was lower at the beginning and in the last five minutes of the test. To see, whether that behavior can be explained by the motion of the piston, the flow versus the piston pressure was plotted which is shown in fig. 7.13. However, this time it is not the performance that is of interest (which makes use differential pressure at the PTS), but the behavior of the flow versus piston pressure. This is shown in fig. 7.16.

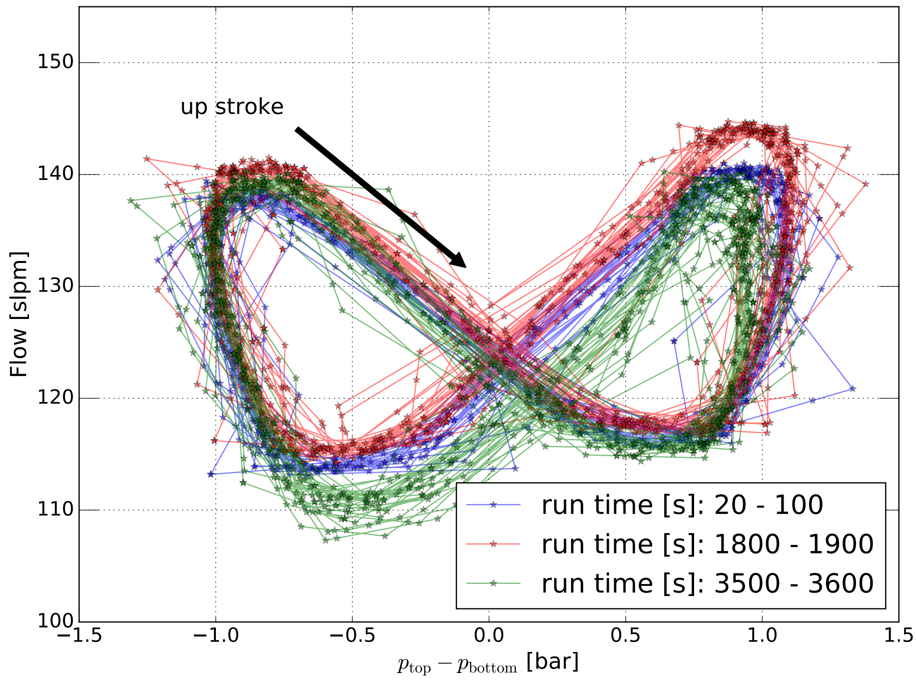

Figure 7.16.: Flow versus piston pressure for beginning, middle and end of the long term test.

Here - unlike in the plot for the performance measurement - the piston pressure is shown with its sign. Thus, the up and down stroke can be identified. On the right-hand side in this plot p_{top} is larger than p_{bottom}. Thus, it contains the sensor values of the top strokes whereas the left-hand side contains the data of the down strokes. The different colors represent the three regions marked in fig. 7.14.

Presumably, the eventual decoupling can be explained by a piston that becomes stuck due to higher friction. The increasing frictional force originates in the bigger thermal expansion of the UHMWPE-gaskets compared to the steel tube (linear coefficients: UHMWPE $\approx 200 \times 10^{-6}\,\text{K}^{-1}$, steel $\approx 15 \times 10^{-6}\,\text{K}^{-1}$). With less displacement due to this trammeled transmission of force, the flow decreases.

Before the long term test, a first decoupling happened at a piston pressure of 1.5 bar after a few minutes of operation. As the pump had not warmed up so quickly, the predominant force for the decoupling was the piston pressure. Furthermore, after the decoupling the conrod could rather easily be moved by hand. This was not possible immediately after the decoupling of the long term test. However, on the next day, the setup was movable by hand again. This confirms the assumption of an expanded and hence clamping piston. Luckily, the piston gaskets appear to have taken no permanent damage. In order to test, whether the warming primarily originates by friction or by the compression, further tests have to be make.

8. Summary and Outlook

8.1. Münster TPC

It has been shown that the Münster TPC is finally ready to take data. With the input plugin for the .eve format for the new data processor PAX and configuration files for the different TPC modes, the base for future analysis and measurements have been made. A new method of gain calibration was suggested using the capabilities of the new data processor PAX . Whether this or the established fixed-window method is favorable will need to be decided. Nevertheless, both might become a useful complement for a combined method. Independent from the used gain calibration, a method for setting the trigger and zero suppression thresholds was presented. This method allows setting the thresholds in units of pe, which is dependent on the gains for the individual PMTs. The next steps will be to further improve analysis and add corrections to the data.
From the simulations (see [12]), a light-collection-efficiency (LCE) map should easily be implemented to be used in PAX . With that, the energy resolution will improve by using up to now unused correction plugins. First and foremost, it allows a better 3D reconstruction which is necessary for positional-dependent energy corrections. Eventually, energy calibrations can be done using external (Cs137) or internal (Kr83m) sources. However, it remains unclear yet, whether the resolution of the 3D reconstruction will be as precise as in the larger TPCs, as there are only 7 PMTs at the top.

8.2. Xenon Pump

The now finished xenon pump has shown good performance for differential pressures up to 1 bar. The new pair of gaskets has a much smaller bypass flow than with the old gaskets. In fact, the leakage rate was reduced to 9.4 slpm/bar. Concerns about evacuating the dead volume in between the gaskets luckily turned out to be no issue.
Furthermore, the flapper valves have been improved. They are made of thicker spring steel and have a bigger surface than the original ones. In the previous design, the flapper valves were pressed into the holes they should seal, which led to permanent deformation. The current design includes the hole being supported by a grid. In a leakage test, the new flappers proved a slower pressure drop compared to the old pair of gaskets despite of the larger design.

Unfortunately, the pump is still limited by the magnetic coupling. This will be improved soon by 10x20x20 mm bar magnets for a new outer ring. A simulation showed (see fig. A.1) that with the new ring an additional force of nearly 900 N will be available.

A risk of decoupling will thus be reduced. Furthermore, the pump might be able to run at higher speeds. For the time being it is not possible to run it at full speed as the piston pressure increases to fast. The planned new ring is likely to be the last upgrade of this type, as even bigger outer rings will neither be practical nor efficient anymore. A different approach using specific controlled coils instead of a mechanically moved ring is being designed at RPI but is yet in an early state. Simultaneously, a setup using a linear motor instead of an AC drive is under development. This approach reduces torque and promises less maintenance.
It was shown, that for a reasonable set of parameters, the peak flow rate has to be almost 600 slpm (fig. 7.3). Larger pipes than the 1/2" lines would be a mayor improvement as the currently used pipes are presumably the main resistance.
A long term test failed - probably due to a warming of the piston gaskets after only one hour. The higher thermal expansion of the piston gasket's material compared to the tube's expansion led to an increased friction at higher temperatures. Eventually, the maximum coupling force to the ring was exceeded, leading to a decoupling of the two components. Whether the warming primarily comes from the friction or the compression will be tested soon. In order to do so, a temperature sensor will be put directly into the cylinder. Nevertheless, another redesign of the piston gaskets and/or a suitable cooling method is unavoidable. Subsequently, long-term measurements for abrasion need to be done to check the gasket's sealing over time. Only if the maintenance intervals to change the gaskets are in long periods, the pump can be used for large-scale experiments like XENON1T.

Eventually, a measurement for purity has yet to be done. The aim was to have a high-purity xenon pump. Although only clean components have been used for this prototype, they have not been screened for impurities yet. Theoretically, there should not be any part which could not be replaced by a cleaner one in case of a conspicuous screening result.

9. Bibliography

[1] Clowe, D. et al.: "A Direct Empirical Proof of the Existence of Dark Matter". In: *ApJ Letters in press* 648 (Sept. 2006), pp. L109–L113. DOI: 10.1086/508162. eprint: astro-ph/0608407.

[2] Planck Collaboration et al.: "Planck 2015 results. XIII. Cosmological parameters". In: *ArXiv e-prints* (Feb. 2015). arXiv: 1502.01589.

[3] LUX Collaboration et al.: "Improved WIMP scattering limits from the LUX experiment". In: *ArXiv e-prints* (Dec. 2015). arXiv: 1512.03506.

[4] Aprile, E. and XENON1T collaboration: "The XENON1T Dark Matter Search Experiment". In: *ArXiv e-prints* (June 2012). arXiv: 1206.6288 [astro-ph.IM].

[5] XENON Collaboration: Elena Aprile: "The XENON Dark Matter Experiment". In: *ArXiv Astrophysics e-prints* (Feb. 2005). eprint: astro-ph/0502279.

[6] Xenon100 Collaboration et al.: "The XENON100 dark matter experiment". In: *Astroparticle Physics* 35 (Apr. 2012), pp. 573–590. DOI: 10.1016/j.astropartphys.2012.01.003. arXiv: 1107.2155 [astro-ph.IM].

[7] Aprile, E. et al.: "Dark Matter Results from 225 Live Days of XENON100 Data". In: *Physical Review Letters* 109.18, 181301 (Nov. 2012), p. 181301. DOI: 10.1103/PhysRevLett.109.181301. arXiv: 1207.5988 [astro-ph.CO].

[8] The XENON collaboration et al.: "Physics reach of the XENON1T dark matter experiment". In: *ArXiv e-prints* (Dec. 2015). arXiv: 1512.07501 [physics.ins-det].

[9] Solovov, V. N. et al.: "Measurement of the refractive index and attenuation length of liquid xenon for its scintillation light". In: *Nuclear Instruments and Methods in Physics Research A* 516 (Jan. 2004), pp. 462–474. DOI: 10.1016/j.nima.2003.08.117. eprint: physics/0307044.

[10] Aprile, E. and Doke, T.: "Liquid xenon detectors for particle physics and astrophysics". In: *Reviews of Modern Physics* 82 (July 2010), pp. 2053–2097. DOI: 10.1103/RevModPhys.82.2053. arXiv: 0910.4956 [physics.ins-det].

[11] Kubota, S. et al.: “Dynamical behavior of free electrons in the recombination process in liquid argon, krypton, and xenon”. In: *Phys. Rev. B* 20 (8 Oct. 1979), pp. 3486–3496. DOI: 10.1103/PhysRevB.20.3486. URL: http://link.aps.org/doi/10.1103/PhysRevB.20.3486.

[12] Althüser, L.: “GEANT4 simulations of the Muenster dual phase xenon TPC”. Bachelor thesis. Institut für Kernphysik, Westfälische Wilhelms-Universität Münster, Sept. 2015.

[13] Schulz, J.: “Design of a 2-Phase Xenon Time Projection Chamber for Electron Drift Length Measurements”. Diploma thesis. Institut für Kernphysik, Westfälische Wilhelms-Universität Münster, Dec. 2014.

[14] Levy, C.: “Light Propagation and Reflection off Teflon in Liquid Xenon Detectors for the XENON100 and XENON1T Dark Matter Experiments”. Dissertation. Institut für Kernphysik, Westfälische Wilhelms-Universität Münster, 2014.

[15] Blanke, J.: “Implementation of a Fiberglass Feed-Through into the Muenster Time Projection Chamber for the Calibration of the Photomultipliers using a LED pulser”. Bachelor thesis. Institut für Kernphysik, Westfälische Wilhelms-Universität Münster, Dec. 2015.

[16] *Tektronix 3000 series datasheet.* Mar. 23, 2016. URL: http://www.tek.com/datasheet/afg3000-series.

[17] Rosendahl, S.: “Gas purification of the XENON dark matter search”. PhD Thesis. Westfälische Wilhelms-Universität Münster, Institut für Kernphysik, 2015.

[18] Kastens, L. W. et al.: “Calibration of a liquid xenon detector with Kr83^{m}”. In: *Physical Review C* 80.4, 045809 (Oct. 2009), p. 045809. DOI: 10.1103/PhysRevC.80.045809. arXiv: 0905.1766 [physics.ins-det].

[19] Jones, E., Oliphant, T., Pterson, P., et al.: *SciPy: Open source scientific tools for Python.* version = 0.17.0, [Online; accessed 2016-04-08]. 2001–. URL: http://www.scipy.org/.

[20] Schulte, D.: “Capacitance-Based Levelmeter Read-Out for the Münster Dual Phase Xenon Time Projection Chamber”. Bachelor thesis. Institut für Kernphysik, Westfälische Wilhelms-Universität Münster, Mar. 2016.

[21] Xenon collaboration internal wiki: *222Rn emanation test of the QDrive pump from Muenster.* Oct. 2012.

[22] LePort, F. et al.: “A magnetically driven piston pump for ultra-clean applications”. In: *Review of Scientific Instruments* 82.10 (Oct. 2011), pp. 105114–105114. DOI: 10.1063/1.3653391. arXiv: 1104.5041 [physics.ins-det].

[23] Buß, A.: “Design and test to construct a magnetically driven piston pump for high-purity xenon experiments”. Bachelorthesis. Institut für Kernphysik, Westfälische-Wilhelms-Universität, Oct. 7, 2013.

[24] Bronštejn, I., Musiol, G., and Mühlig, H.: *Taschenbuch der Mathematik*. Deutsch, 2008. ISBN: 9783817120079. URL: `https://books.google.de/books?id=VnsL9p8hXfQC`.

[25] Fitzgibbon, A., Pilu, M., and Fisher, R. B.: “Direct least square fitting of ellipses”. In: *Pattern Analysis and Machine Intelligence, IEEE Transactions on* 21.5 (1999), pp. 476–480.

[26] White, F. M.: *Fluid Mechanics*. 7th edition. McGraw-Hill, 2011. ISBN: 978-0-07-352934-9.

A. Appendix

Table A.1.: reduced χ^2 for gains in fig. 4.3.

Channel	χ^2/ndof
0	4.40
1	1.62
2	2.33
3	1.80
4	1.33
5	4.38
6	18.09
7	11.80
8	16.07
9	9.43
10	3.00
11	2.55
12	5.21
13	1.30

A-A (1 : 1)

B-B (1 : 1)

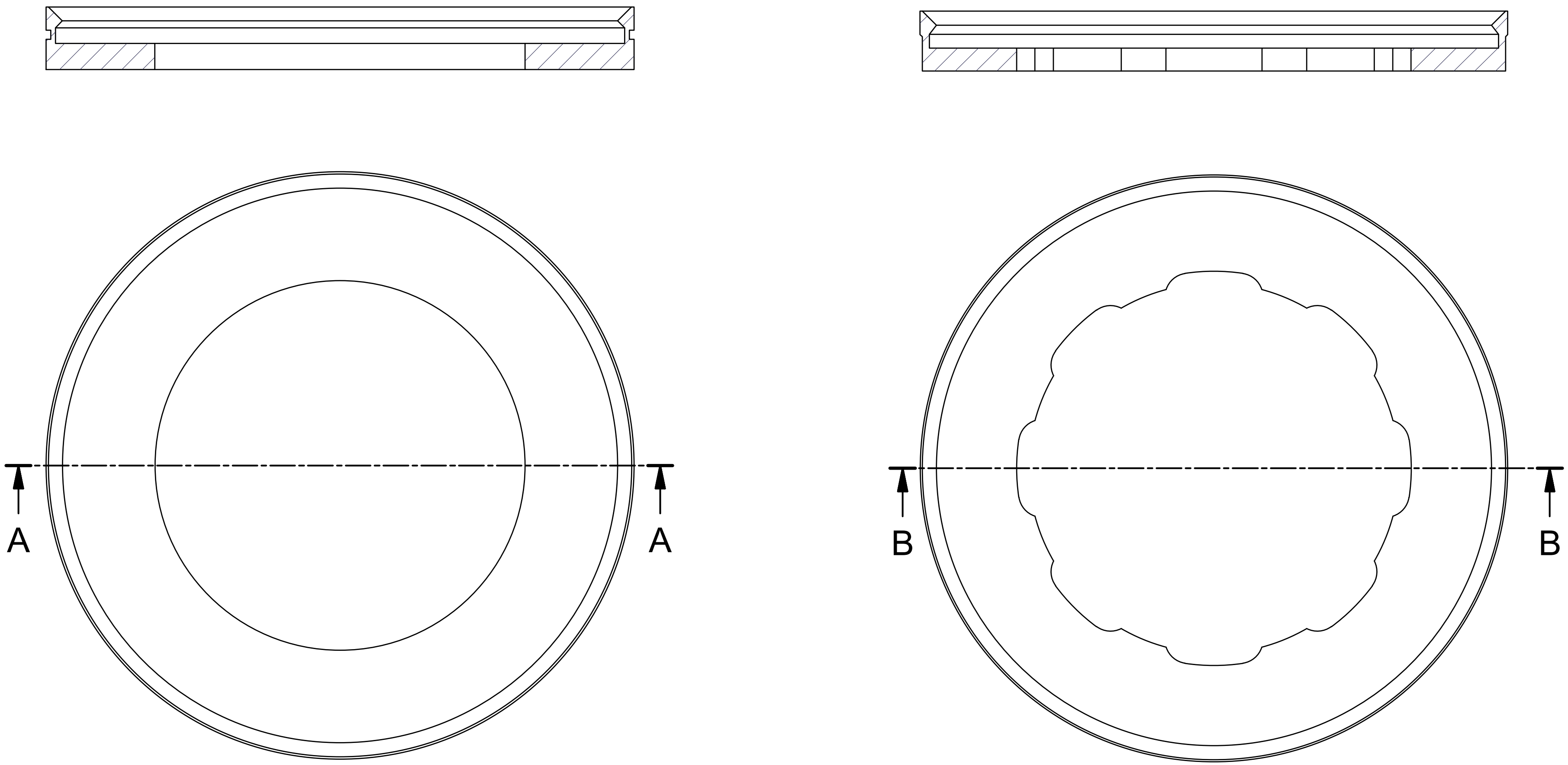

Westfälische Wilhelms-Universität Münster		Maßstab : 1 : 1	Werkstoff : Polyethylen, hohe Dichte
		BG:	Pos. Nr. : / Anzahl :
	Datum	Name	
Gezeichnet	05.04.2016	chuhm_01	
Kontrolliert			
Norm			
Revisionsnr.	V3		
Institut für Kernphysik Wilhelm-Klemm-Str. 9 48149 Münster		Gasket_new_vs_old	1 / A3

Status	Änderungen	Datum	Name

Xe XENON Dark Matter Project

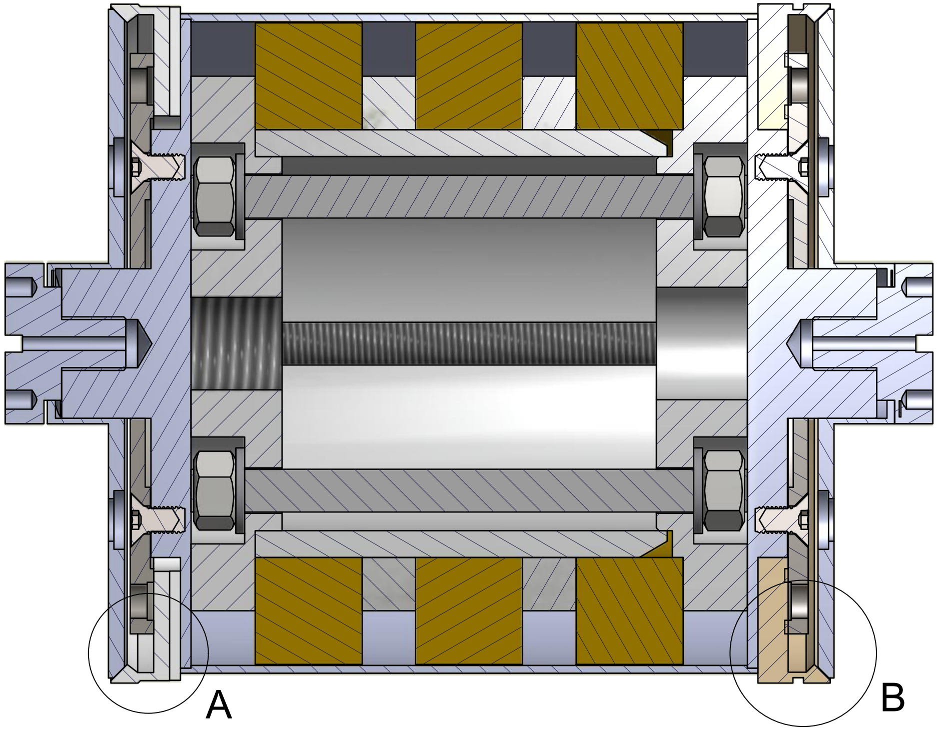

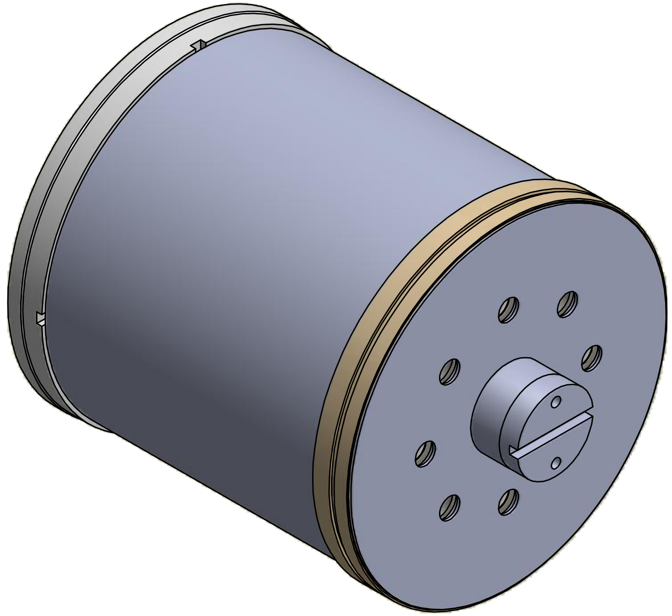

A (3: 1)

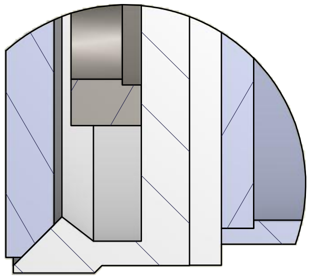

B (3:1)

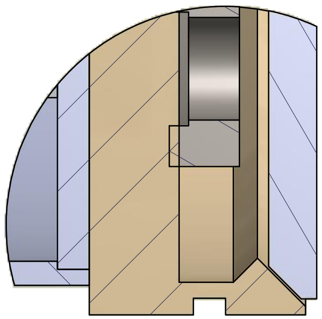

Westfälische Wilhelms-Universität Münster		Maßstab : 1 : 1	Werkstoff :
		BG:	Pos. Nr. : / Anzahl :

	Datum	Name
Gezeichnet	05.04.2016	chuhm_01
Kontrolliert		
Norm		
Revisionsnr.	V3	

Status	Änderungen	Datum	Name

Institut für Kernphysik
Wilhelm-Klemm-Str. 9
48149 Münster

Xe XENON Dark Matter Project

Gasket_new_vs_old

2

A3

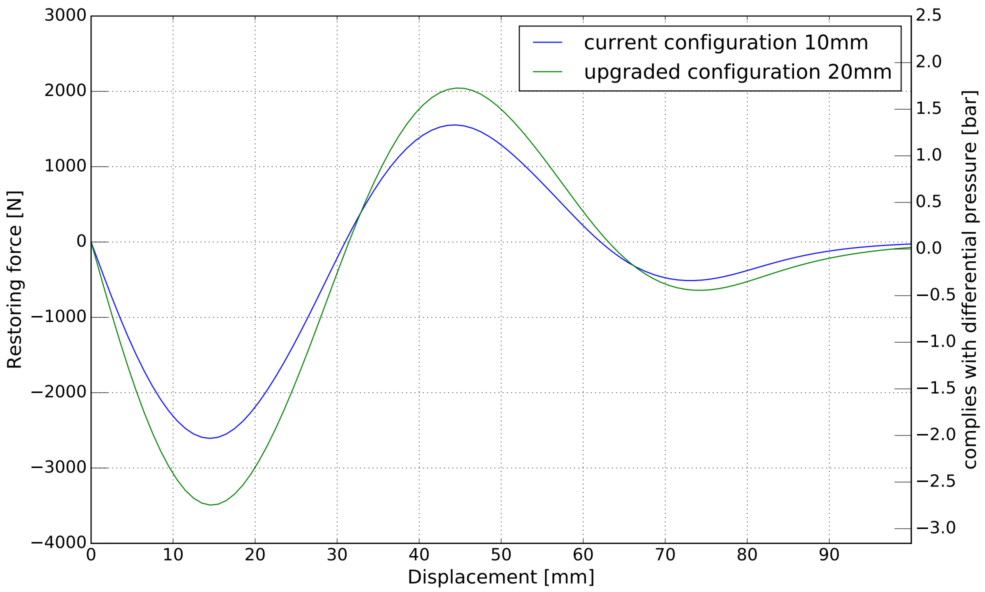

Figure A.1.: Simulations of restoring force for current and upgraded configuration. The simulation was adapted from [23] for the planned upgrade.

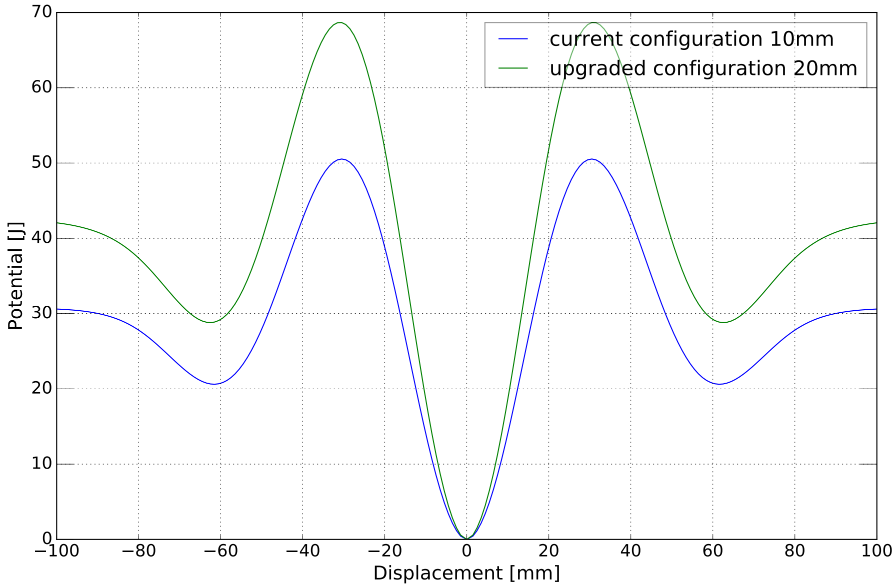

Figure A.2.: Potential of restoring forces.

The .eve file format

Axel Buß

April 4, 2016

Introduction

The data acquisition used for TPC at Münster University is done by the program FPPGUI written by Dr. Volker Hannen. This document is meant to be a technical manual for the file format to help implementing input routines in future software. I've tried to make it as clear as possible and rather repeat some things than leaving something out.

1 Data Acquisition - caen1724.par

The data acquisition parameters are defined in the file:
`~/sisdaq/Parameter/caen1724.par` [1]
The file contains several parameters to control the caen1724 boards. In the appendix you can find a typical caen1724.par file. The parameters most likely to be changed are:

- **number of modules** : 0..20
- **page size** : 0..10
  - 0 = 512k
  - 1 = 256k
  - 2 = 128k
  - 3 = 64k
  - 4 = 32k
  - 5 = 16k
  - 6 = 8k
  - 7 = 4k
  - 8 = 2k
  - 9 = 1k
  - 10 = 512
- **post_trigger_samples** : 0..N (*ends with event anyway*)
- **enable_external_trig** : 0,1
- **trigger_coinc_level** : 1..N (*number of channels needed to trigger*)
- **zero length_encoding** : 0,1
- **zle_nlbk** : 0..N (*number of "look back" words*)

[1] The path of the sysdaq folder might be located somewhere else

- **zle_nlfw** : 0..N (*number of "look forward" words*)
- individual channel settings, containing:
  - **Channel_active** 0,1 (x8)
  - **Thresholds** $0..2^{14}-1$ (x8)
  - **Baseline** $0..2^{14}-1$ (x8)
  - **ZS_Threshold** $0..2^{14}-1$ (x8)
  - **Zero_offset** $0..2^{14}-1$ (x8)

2 Reading binary data - The .eve File Format

2.1 file header

Each .eve file begins with a file header. The file header is built out of 8 words containing unsigned 32bit integers. However the last 4 words of this header are not used and only contain the hexadecimal dummy value "0xaffe".

The timestamp is the ordinary unix timestamp with second precision. Each event has

<table>
<tr><td>31</td><td>30</td><td>29</td><td>28</td><td>27</td><td>26</td><td>25</td><td>24</td><td>23</td><td>22</td><td>21</td><td>20</td><td>19</td><td>18</td><td>17</td><td>16</td><td>15</td><td>14</td><td>13</td><td>12</td><td>11</td><td>10</td><td>9</td><td>8</td><td>7</td><td>6</td><td>5</td><td>4</td><td>3</td><td>2</td><td>1</td><td>0</td></tr>
<tr><td colspan="32">BYTE ORDER</td></tr>
<tr><td colspan="32">VERSION</td></tr>
<tr><td colspan="32">BUFFSIZE</td></tr>
<tr><td colspan="32">TIMESTAMP</td></tr>
<tr><td colspan="32"><not used>(0xaffe)</td></tr>
<tr><td colspan="32"><not used>(0xaffe)</td></tr>
<tr><td colspan="32"><not used>(0xaffe)</td></tr>
<tr><td colspan="32"><not used>(0xaffe)</td></tr>
</table>

Table 1: file header in 32bit register

its an own more precise timestamp. After this file header the data from the *caen* boards starts with an event header.

```
[("event_size", "<u4"),
 ("event_type", "<u4"),
 ("event_timestamp", "<i4")]
```

Listing 1: Event Header

emphevent_size is the length in words of the current event including the header itself. The type of the event can be classified by *event_type* which will be a 4 for a meta data event and later a 3 for a signal event. As the file just has started , this will not be a signal event but a meta data event which continues basically with a copy of the *caen1724.par* file.

```
[("no_mod", "<i4"),
("base", "<20u4"),
("downsample_factor", "<i4"),
("page_size", "<i4"),
```

```
("post_trigger_samples", "<i4"),
("enable_external_trig", "<i4"),
("trigger_logic", "<i4"),
("trigger_coinc_level", "<i4"),
("trigger_n_quartets", "<i4"),

("zle", "<i4"),  # zero length encoding
("zle_logic", "<i4"),  # zle, positive(0) or negative(1) logic
("zle_nlbk", "<i4"),  # zle, number of look back words
("zle_nlfwd", "<i4"),  # zle, number of look forward words

("integrate_signals", "<i4"),
("substract_offset", "<i4"),

("chan_active", "<(20,8)i4"),
("chan_dac", "<(20,8)u4"),
("threshold", "<(20,8)i4"),
("zs_threshold", "<(20,8)i4"),
("zero_offset", "<(20,8)i4"),

("nof_active_channels", "<20i4"),  # 0...8, number of active channels on each caen board
("nof_samples", "<u4"),  # Redundant with page size Only 512 instead of 10
("event_count", "<i4")]
```

The 20 you can see at some places in this code is a hardcoded limit for a maximum number of flash ADCs. When fewer modules are connected the remaining values are filled up with zeros.

The next event probably is a signal event. After another header like Listing 1 the actual signal header begins. The *event_size* gives the length of the whole event including all boards. Whether you have zero length encoding enabled or disabled is at this point not important yet, as the headers do not differ that much.

The data however does. In figure 1 you can see how a signal event is constructed. The header consists of 4 words with different fields. By selecting the desired fields with shift and bitwise logical operations the information can be obtained. Keep the according lines of code well commented so that is understandable for others.

The *EVENT SIZE* here represents the number of words only for this board. The next board will start with its own header after that. The *TRIGGER TIME TAG* is the precise timestamp of this event. As the Flash ADC has 14bit precision, 2 samples fit into one word, leaving 4 bits unused. In the case of disabled zero length encoding all channels have a fixed number of samples/words. When the first (zeroth) channel is read, the next enabled channel starts with the same number of samples/words and so on. After the last enabled channel the next board's signal header comes along. There is no extra event header whatsoever. When the last module is read the event closes with a last word containing "0xaffe". After that the next event header begins unless the end of file is reached.

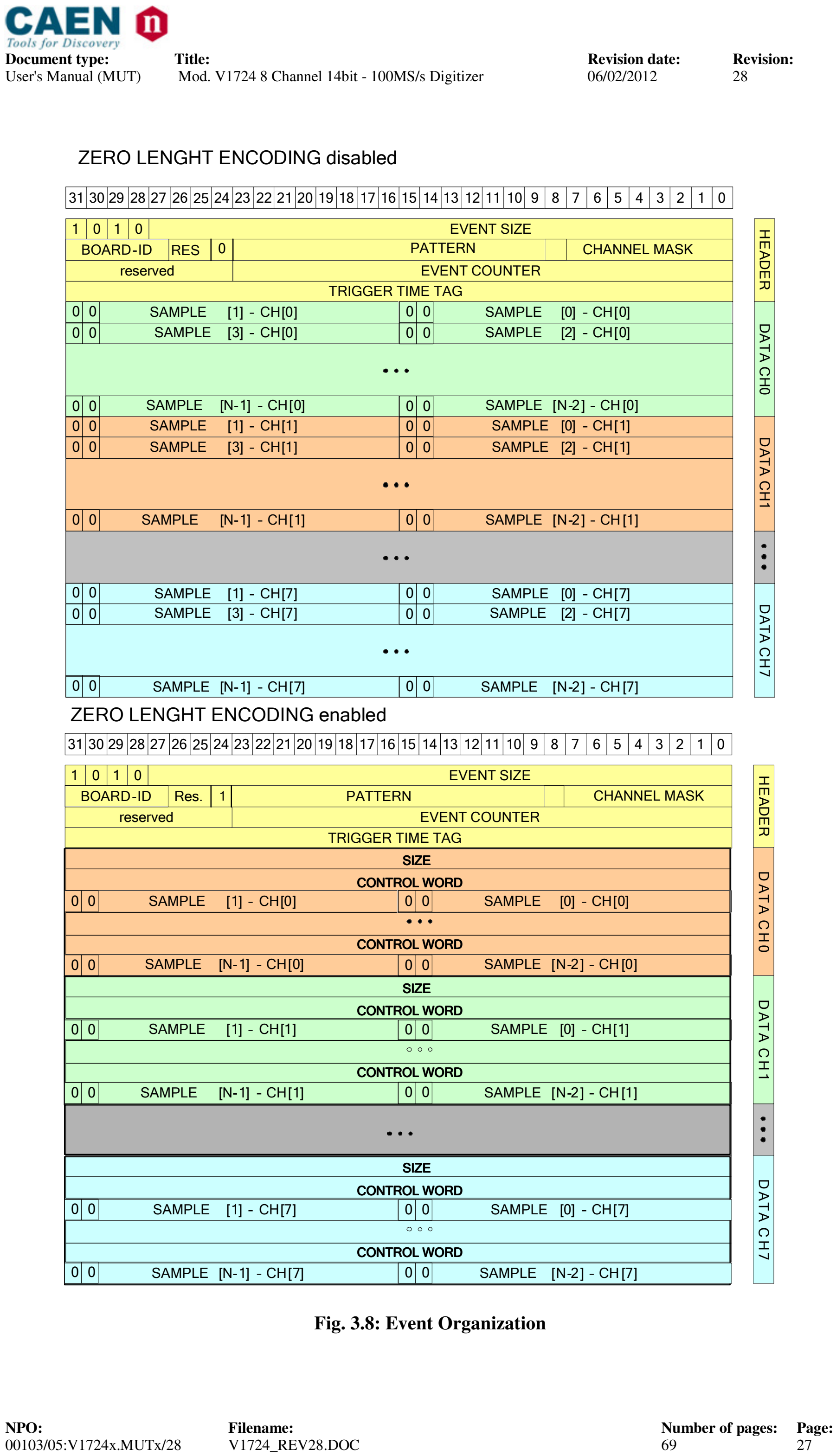

Figure 1: Event organisation after event header. While the headers are very similar (except one bit), the data organisation differs drastically. (From caen1724 manual)

Listing A.1: "MSTPC_dualphase.ini"

```
# This configuration file is adapted from XENON100.ini for the Münster TPC
# It will contain MünsterTPC-specific details
# date: Aug 26th 2015
# editor : Axel Buß

[pax]
parent_configuration = "_base"
plugin_paths = ['examples/muenster']

input = 'EVE_file.EveInput'
#show_waveforms = ['ShowWaveforms.PlotAllChannels']
#output = 'Plotting.PlotEventSummary'
# Global settings, passed to every plugin
dsp = [
            # Do some sanity checks / cleaning on pulses
            #'CheckPulses.SortPulses',
            'CheckPulses.ConcatenateAdjacentPulses',
            'CheckPulses.CheckBounds',

            # Find individual hits
             'HitFinder.FindHits',
            # Combine hits into rough clusters = peaks
            'BuildPeaks.GapSizeClustering',
            'NaturalBreaksClustering.NaturalBreaksClustering',

            # Reject hits in noisy channels
            'RejectNoiseHits.RejectNoiseHits',
            'SumWaveform.SumWaveform', # Must do this AFTER noisy hit rejection!

            # Compute sum-waveform and hit-dependent properties for each peak
            'BasicProperties.BasicProperties',
            'BasicProperties.SumWaveformProperties',
            'BasicProperties.CountCoincidentNoisePulses'
        ]

# Compute peak properties: can be redone from processed data file
compute_properties = [
                        'RobustWeightedMean.PosRecRobustWeightedMean',
                        'WeightedSum.PosRecWeightedSum',
                        'MaxPMT.PosRecMaxPMT',
# 'NeuralNet.PosRecNeuralNet',
# 'ChiSquareGamma.PosRecChiSquareGamma',
# 'HitpatternSpread.HitpatternSpread',
                    ]

# Final stage with 'risky' operations: peak classification, S1/S2 pairing, corrections
# Intentionally last, so reclassification takes least work
pre_analysis = [
                # Classify the clusters based on the properties
                'ClassifyPeaks_gastpcms.AdHocClassification',

                # Combine S1 and S2 into pairs = interactions and compute properties
                # which depend on S1 AND S2 specific information (i.e. z-corrections)
                 'BuildInteractions.BuildInteractions',
# 'BuildInteractions.BasicInteractionProperties',
              ]
pre_output = []
#output = 'Table.TableWriter'

[DEFAULT]
tpc_name = "MuensterTPC"



# Time in the event at which trigger occurs. Set to None or leave out if there is no trigger
trigger_time_in_event = 72000 * ns # Check settings in caen1724.par

pmt_0_is_fake = False # TODO

# Detector specification
# PlotChannelWaveform2D expects the detector names' lexical order to be the same as the channel order
channels_in_detector = {
                      'tpc': [0, 1, 2, 3, 4, 5, 6,
                              7, 8, 9, 10, 11, 12, 13]
                      }
n_channels = 14 # 2x v1724

# PMT numbers for tpc, specified as lists

channels_bottom = [0, 1, 2, 3, 4, 5, 6]
channels_top = [7, 8, 9, 10, 11, 12, 13]
```

```
# PMT locations taken from technical drawing of Muenster TPC
# Whether they are in correct order has to be confirmed yet
# Note: don't forget the units...
tpc_length = 17 * cm
tpc_radius = 4 * cm
pmt_locations = [
               {'x': -2.900 * cm, 'y': -1.450 * cm}, # 0 bottom
               {'x': -2.900 * cm, 'y': +1.450 * cm}, # 1
               {'x': 0.000 * cm, 'y': +2.900 * cm}, # 2
               {'x': 0.000 * cm, 'y': 0.000 * cm}, # 3
               {'x': 0.000 * cm, 'y': -2.900 * cm}, # 4
               {'x': 2.900 * cm, 'y': -1.450 * cm}, # 5
               {'x': 2.900 * cm, 'y': 1.450 * cm}, # 6
               {'x': -2.900 * cm, 'y': -1.450 * cm}, # 7 top
               {'x': -2.900 * cm, 'y': +1.450 * cm}, # 8
               {'x': 0.000 * cm, 'y': +2.900 * cm}, # 9
               {'x': 0.000 * cm, 'y': 0.000 * cm}, # 10
               {'x': 0.000 * cm, 'y': -2.900 * cm}, # 11
               {'x': 2.900 * cm, 'y': -1.450 * cm}, # 12
               {'x': 2.900 * cm, 'y': 1.450 * cm}, # 13
               ]

# gains obtained bz Axel Buss 15.02.16 in cold state
gains =
    [3123758.1521910313,
     2963517.4613321265,
     2593233.1311770072,
     2780521.5353519521,
     3813631.0951762595,
     1008164.4778156757,
     2211680.9222973068,
     2529746.5243497416,
     2250531.0233015493,
     3641299.3599790633,
     2756464.4527533087,
     2176674.6927838745,
     3068637.1272498947,
     2954521.8463605698]

gain_sigmas =
     [1348474.5161715674,
     1378260.3575948703,
     1221711.0758821992,
     1387667.973132777,
     1831679.2635322467,
     223837.66514235115,
     907697.56491794379,
     935469.48858005437,
     882978.05700240226,
     1439581.3710307193,
     1114661.6708463638,
     958053.64191821881,
     1367045.6526938593,
     1375199.2654498301]

[EVE_file.EveInput]
Channel_to_PMT_mapping =
    {0 : 0, 1 : 1, 2 : 2, 3 : 3, 4 : 4, 5 : 5, 6 : 6, 7 : 7,
    8 : 8, 9 : 9, 10 : 10, 11 : 11, 12 : 12, 13 : 13}

[Plotting]
waveforms_to_plot = (
                   {'internal_name': 'tpc', 'plot_label': 'TPC (hits only)',
                   'drawstyle': 'steps', 'color':'black'},
                   )
[HitFinder.FindHits]
# Compute baseline on first n samples in pulse:
initial_baseline_samples = 20 # When using ZLE this must not be higher than 2x zle_nlbk as the peaks will be counted in otherwise
height_over_noise_high_threshold = 6
height_over_noise_low_threshold = 2
# Compute baseline on first n samples in pulse:

# Max hits to look for in each pulse: rest will be ignored
max_hits_per_pulse = 500

# Diagnostic plots settings
make_diagnostic_plots = 'never' # Can be always, never, tricky cases, no hits, hits only, saturated
make_diagnostic_plots_in = 'hitfinder_diagnostic_plots'
# Add extra information to diagnostic plots - this gives info on sum of hits in one pulse
diagnostic_plot_info = 'yes' # can be yes or no

# Threshold 2: Absolute ADC counts above baseline
absolute_adc_counts_high_threshold = 1 # ADC counts
```

```
absolute_adc_counts_low_threshold = 1 # ADC counts


# Threshold 3: - Height / minimum
height_over_min_high_threshold = 2
height_over_min_low_threshold = 0

# Raise low threshold temporarily to fraction of hit height for rest of pulse
dynamic_low_threshold_coeff = 0.01


[Cluster]
# Suspicious channel rejection settings
penalty_per_noise_pulse = 1 # "pe" equivalent penalty
penalty_per_lone_hit = 1 # "pe" equivalent penalty
# Threshold to mark a suspicious channel
penalty_geq_this_is_suspicious = 3 # "pe" equivalent penalty

# If the ratio of noise channels / contributing channels is larger than this, classify peak as 'noise'
# noise channel = a channel in the same detector which shows data, but doesn't contribute to the peak
# (or only hits rejected by the suspicious channel algorithm)
max_noise_channels_over_contributing_channels = 2

[Cluster.MeanShift]
s2_size = 20
# If spe peaks are separated by less than this, they will be clustered together
s2_width = 1.0 * us
p_value = 0.999
cluster_all = True

[Cluster.HitDifference]
max_difference = 2 * ns

[BuildInteractions.BuildInteractions]
# Pair S1s and S2s in order of size, but no more than these:
pair_n_s2s = 5
pair_n_s1s = 3

# Never pair S2s smaller than:
s2_pairing_threshold = 70 # pe

# Preference in algorithms to use for the xy reconstructed position
xy_posrec_preference = ['PosRecWeightedSum','PosRecMaxPMT']


[BuildInteractions.BasicInteractionProperties]
# Add 'zombie PMTS' here (only effective if active_saturation_and_zombie_correction = True)
# These are PMTs who have died, but the loss of light yield has not yet been accounted for in the overall S1 or S2
# light yield map. These PMTs will be treated just like saturated PMTs: when computing the corrected area,
# the observed area in the zombie channels (which will be 0) is replaced by the expected area based on the other PMTs.
# DO NOT keep PMTs here after the light yield maps have been fixed!!!
# If you don't understand why, stop modifying the file and just fix the light yield map!
zombie_pmts_s1 = []
# S2 zombie PMTs will only work on the top, as we have no S2(x,y,pmt) patterns for the bottom array.
# For now, all dead top PMTs are included for the S2, since we don't have the S2(x, y) light yield in pax yet...
zombie_pmts_s2 = []


[NaturalBreaksClustering]
# Points in log10(peak_area), goodness_of_split. Split threshold is linearly interpolated between these.
# Manual "fit" to stay above 99.9th percentile of a menagerie of signals -- see this note:
# xenon:xenon1t:processor:natural_breaks_clustering
split_goodness_threshold = ([0, 1.5, 2.5, 3, 3.5, 9], [1, 0.8, 0.51, 0.46, 0.44, 0.44])

# Minimum gap between hits to qualify as a break:
# This means there must be a certain time with no hits at all.
# If you set this to 0,
# + you will be probably be able to split double scatter S2s at high-energy.
# 0 overlapping peaks become possible;
# - you will see weird results in the electron train after large S2s (e.g. lots of s1s found);
# - the performance drops sharply (because every split point between hits now needs to be tested)
min_gap_size_for_break = 10 * ns

[BuildPeaks.GapSizeClustering]
# Start a new cluster / peak if a gap larger than this is encountered
# see [note tbd]
max_gap_size_in_cluster = 20 * ns

[RejectNoiseHits]
# Suspicious channel rejection settings
penalty_per_noise_pulse = 0 # "pe" equivalent penalty
penalty_per_lone_hit = 1 # "pe" equivalent penalty
```

```
# Threshold to mark a suspicious channel
penalty_geq_this_is_suspicious = 3 # "pe" equivalent penalty

# Very dodgy channels start with a base penalty to make them always suspicious
# This means they will contribute only if non-suspicious channels in the same detector show > 3pe area
# Dodgy channels selected using run 10 noisy AmBe (120402_2000)
base_penalties = {
                }


[Table.TableWriter]
#output_format = 'hdf5_pandas' # hdf5, csv, numpy, html, json, root, hdf5_pandas
# Don't leave out hits and pulses -- that's what we're after!
fields_to_ignore = ['sum_waveforms',
                    'channel_waveforms',
                    #'all_hits',
                    'raw_data',
                    'hits',
                    #'pulses',
                    'detector',
                    'n_reconstructed_positions',
                    'reconstructed_positions_start',
                    'area_fraction_top',
                    'area_midpoint',
                    'area_per_channel',
                    'birthing_split_fraction',
                    'birthing_split_goodness',
                    'bottom_hitpattern_spread',
                    'hit_time_mean',
                    'hit_time_std',
                    'hits_fraction_top',
                    'interior_split_fraction',
                    'interior_split_goodness',
                    'left',
                    'lone_hit_channel',
                    'mean_amplitude_to_noise',
                    #'n_hits',
                    'n_noise_pulses',
                    #'n_saturated_channels',
                    #'n_saturated_per_channel',
                    #'n_saturated_samples',
                    #'range_area_decile',
                    'right',
                    'sum_waveform',
                    'sum_waveform_top',
                    'top_hitpattern_spread',
                    ]

[WaveformSimulator]
# ...
"""
WavefromSimulator settings are necessary to run pax, even though the module is not used for processing later on.
For processing all files in this thesis, values for XENON100 were inserted here as a placeholder.
"""
[BasicProperties.SumWaveformProperties]
# Length of the peak sum waveform field.
# Must be an even multiple of sample size, pax will add 1 sample width so there is a clear center.
peak_waveform_length = 2.5 * us

[RobustWeightedMean.PosRecRobustWeightedMean]
# Remove PMTs that are more than ... away in each step
outlier_threshold = 2.5 # 3 and 2 both seem a little worse, though not much. 1.5 is clearly worse.

# Give up if this number of PMTs (or less) is left
min_pmts_left = 3

# Outer ring PMTs are partially obstructed by the TPC wall, upweigh their areas to compensate
outer_ring_pmts = []
outer_ring_multiplication_factor = 1.5
```

Listing A.2: "MSTPC_gaincal.ini"

```
# This configuration file is adapted from XENON100.ini for the Münster TPC
# It contains MünsterTPC-specific details
# date: Mar 30 2016
# editor : Axel Buß

[pax]
parent_configuration = "_base"
plugin_paths = ['examples/muenster']

input = 'EVE_file.EveInput'
```

```
#show_waveforms = ['ShowWaveforms.PlotAllChannels']
#output = 'Plotting.PlotEventSummary'
# Global settings, passed to every plugin
dsp = [
           # Do some sanity checks / cleaning on pulses
           #'CheckPulses.SortPulses',
           'CheckPulses.ConcatenateAdjacentPulses',
           'CheckPulses.CheckBounds',

           # Find individual hits
           'HitFinder.FindHits',
           # Combine hits into rough clusters = peaks
           #'BuildPeaks.GapSizeClustering',

           # Reject hits in noisy channels
           #'RejectNoiseHits.RejectNoiseHits',
           #'SumWaveform.SumWaveform', # Must do this AFTER noisy hit rejection!

           # Compute sum-waveform and hit-dependent properties for each peak
           # 'BasicProperties.BasicProperties',
           #'BasicProperties.SumWaveformProperties',
           # 'BasicProperties.CountCoincidentNoisePulses'
       ]
# Compute peak properties: can be redone from processed data file
compute_properties = [
           #'WeightedSum.PosRecWeightedSum',
           #'MaxPMT.PosRecMaxPMT',
           #'RobustWeightedMean.PosRecRobustWeightedMean',
           #'NeuralNet.PosRecNeuralNet',
           #'ChiSquareGamma.PosRecChiSquareGamma',
           #'HitpatternSpread.HitpatternSpread',
           ]

# Final stage with 'risky' operations: peak classification, S1/S2 pairing, corrections
# Intentionally last, so reclassification takes least work
pre_analysis = [
           # Classify the clusters based on the properties
           #'ClassifyPeaks.AdHocClassification',

           # Combine S1 and S2 into pairs = interactions and compute properties
           # which depend on S1 AND S2 specific information (i.e. z-corrections)
           # 'BuildInteractions.BuildInteractions',
           # 'BuildInteractions.BasicInteractionProperties',
             ]
pre_output = []
#output = 'ROOTClass.WriteROOTClass'
output = 'Table.TableWriter'

[DEFAULT]
tpc_name = "MuensterTPC"



# Time in the event at which trigger occurs. Set to None or leave out if there is no trigger
trigger_time_in_event = 2560 * ns # Check settings in caen1724.par

pmt_0_is_fake = False # Conting from 0

# Detector specification
# PlotChannelWaveform2D expects the detector names' lexical order to be the same as the channel order
channels_in_detector = {
                      'tpc': [0, 1, 2, 3, 4, 5, 6,
                               7, 8, 9, 10, 11, 12, 13]
                      }
n_channels = 14 # 2x v1724

# PMT numbers for tpc, specified as lists

channels_bottom = [0, 1, 2, 3, 4, 5, 6]
channels_top = [7, 8, 9, 10, 11, 12, 13]

# PMT locations taken from technical drawing of Muenster TPC
# Whether they are in correct order has to be confirmed yet
# Note: don't forget the units...
tpc_length = 17 * cm
tpc_radius = 4 * cm
pmt_locations = [
               {'x': -2.900 * cm, 'y': -1.450 * cm}, # 0 bottom
               {'x': -2.900 * cm, 'y': +1.450 * cm}, # 1
               {'x': 0.000 * cm, 'y': +2.900 * cm}, # 2
               {'x': 0.000 * cm, 'y': 0.000 * cm}, # 3
               {'x': 0.000 * cm, 'y': -2.900 * cm}, # 4
               {'x': 2.900 * cm, 'y': -1.450 * cm}, # 5
```

```
            {'x': 2.900 * cm, 'y': 1.450 * cm}, # 6
            {'x': -2.900 * cm, 'y': -1.450 * cm}, # 7 top
            {'x': -2.900 * cm, 'y': +1.450 * cm}, # 8
            {'x': 0.000 * cm, 'y': +2.900 * cm}, # 9
            {'x': 0.000 * cm, 'y': 0.000 * cm}, # 10
            {'x': 0.000 * cm, 'y': -2.900 * cm}, # 11
            {'x': 2.900 * cm, 'y': -1.450 * cm}, # 12
            {'x': 2.900 * cm, 'y': 1.450 * cm}, # 13
            ]


# These gains are placeholder for gain calibration
gains = [1] * 14
gain_sigmas = [0.5] * 14

[EVE_file.EveInput]
Channel_to_PMT_mapping =
   {0 : 0,
   1 : 1,
   2 : 2,
   3 : 3,
   4 : 4,
   5 : 5,
   6 : 6,
   7 : 7,
   8 : 8,
   9 : 9,
   10 : 10,
   11 : 11,
   12 : 12,
   13 : 13}

[Plotting]
waveforms_to_plot = (
               {'internal_name': 'tpc', 'plot_label': 'TPC (hits only)',
               'drawstyle': 'steps', 'color':'black'},
               )
[HitFinder.FindHits]
# Compute baseline on first n samples in pulse:
initial_baseline_samples = 100 # When using ZLE this must not be higher than 2x zle_nlbk as the peaks will be counted in otherwise
height_over_noise_high_threshold = 3
height_over_noise_low_threshold = 1.0
# Compute baseline on first n samples in pulse:

# Max hits to look for in each pulse: rest will be ignored
max_hits_per_pulse = 500

# Diagnostic plots settings
make_diagnostic_plots = 'never' # Can be always, never, tricky cases, no hits, hits only, saturated
make_diagnostic_plots_in = 'hitfinder_diagnostic_plots'
# Add extra information to diagnostic plots - this gives info on sum of hits in one pulse
diagnostic_plot_info = 'yes' # can be yes or no

# Threshold 2: Absolute ADC counts above baseline
absolute_adc_counts_high_threshold = 1 # ADC counts
absolute_adc_counts_low_threshold = 1 # ADC counts


# Threshold 3: - Height / minimum
height_over_min_high_threshold = 2
height_over_min_low_threshold = 0

# Raise low threshold temporarily to fraction of hit height for rest of pulse
dynamic_low_threshold_coeff = 0.01


[Cluster]
# Suspicious channel rejection settings
penalty_per_noise_pulse = 1 # "pe" equivalent penalty
penalty_per_lone_hit = 1 # "pe" equivalent penalty
# Threshold to mark a suspicious channel
penalty_geq_this_is_suspicious = 3 # "pe" equivalent penalty

# If the ratio of noise channels / contributing channels is larger than this, classify peak as 'noise'
# noise channel = a channel in the same detector which shows data, but doesn't contribute to the peak
# (or only hits rejected by the suspicious channel algorithm)
max_noise_channels_over_contributing_channels = 2

[Cluster.MeanShift]
s2_size = 20
# If spe peaks are separated by less than this, they will be clustered together
```

```
s2_width = 1.0 * us
p_value = 0.999
cluster_all = True

[Cluster.HitDifference]
max_difference = 2 * ns

[BuildPeaks.GapSizeClustering]
# Start a new cluster / peak if a gap larger than this is encountered
# see [note tbd]
max_gap_size_in_cluster = 10 * ns

[RejectNoiseHits]
# Suspicious channel rejection settings
penalty_per_noise_pulse = 0 # "pe" equivalent penalty
penalty_per_lone_hit = 1 # "pe" equivalent penalty

# Threshold to mark a suspicious channel
penalty_geq_this_is_suspicious = 3 # "pe" equivalent penalty

# Very dodgy channels start with a base penalty to make them always suspicious
# This means they will contribute only if non-suspicious channels in the same detector show > 3pe area
# Dodgy channels selected using run 10 noisy AmBe (120402_2000)
base_penalties = {
               }


[Table.TableWriter]
#output_format = 'hdf5_pandas' # hdf5, csv, numpy, html, json, root, hdf5_pandas
# Don't leave out hits and pulses -- that's what we're after!
fields_to_ignore = ['sum_waveforms',
                 'channel_waveforms',
                 #'all_hits',
                 'raw_data',
                 'hits',
                 'peaks',
                 #'pulses',
                 'detector',
                 'n_reconstructed_positions',
                 'reconstructed_positions_start',
                 'area_fraction_top',
                 'area_midpoint',
                 'area_per_channel',
                 'birthing_split_fraction',
                 'birthing_split_goodness',
                 'bottom_hitpattern_spread',
                 'hit_time_mean',
                 'hit_time_std',
                 'hits_fraction_top',
                 'interior_split_fraction',
                 'interior_split_goodness',
                 'left',
                 'lone_hit_channel',
                 'mean_amplitude_to_noise',
                 'n_hits',
                 'n_noise_pulses',
                 'n_saturated_channels',
                 'n_saturated_per_channel',
                 'n_saturated_samples',
                 'range_area_decile',
                 'right',
                 'sum_waveform',
                 'sum_waveform_top',
                 'top_hitpattern_spread',
                 ]

[WaveformSimulator]
# ...
"""
WavefromSimulator settings are necessary to run pax, even though the module is not used for processing later on.
For processing all files in this thesis, values for XENON100 were inserted here as a placeholder.
"""
[BasicProperties.SumWaveformProperties]
# Length of the peak sum waveform field.
# Must be an even multiple of sample size, pax will add 1 sample width so there is a clear center.
peak_waveform_length = 2.5 * us
```

Danksagung

An dieser Stelle möchte ich allen danken, die mich während der Arbeit unterstützt haben.
Zunächst geht mein Dank an Prof. Dr. C. Weinheimer. Es war faszinierend an einem Experiment beteiligt gewesen zu sein, das im Falle einer Entdeckung uns ein tieferes Verständnis für unser Universum liefern könnte. Die Möglichkeit mit der Münster TPC die Funktionsweise eines solchen Experiments selbst erforschen zu können war einmalig. Auch die Fortführung der Konstruktion der Xenonpumpe hat mir letztendlich mehr Spaß gemacht, als ich zunächst gedacht hätte. Auch wenn ich nicht länger am Xenonprojekt beteiligt sein werde, so werde ich doch gespannt sein auf das geplante Upgrade. An dieser Stelle danke ich auch schon mal für die Möglichkeit in Ihrer Arbeitsgruppe zu promovieren.
Herrn Prof. Dr. J. Wessels danke ich für die Bereitschaft Zweitkorrekteur dieser Arbeit zu sein.
Als nächstes möchte ich Michael Murra und Alexander Fieguth danken. Stets habt ihr euch Zeit für meine Fragen und habt mir mit Verbesserungsvorschlägen für diese Arbeit einen nicht selbstverständlichen Gefallen getan.
Auch möchte ich unserem Ingenieur Christian Huhmann danken. Nur durch dich wurde seit meiner Zeit als Bachelorstudent die Xenonpumpe zu der, die sie heute ist. Ohne gegenseitiges Achtsamkeit bei der Montage des Rings hätte vielleicht einer von uns beiden einen Finger weniger. Danke auch für die stets schnelle Bereitstellung von den Bildern für diese Arbeit.
Ich danke auch den beiden Werkstätten für die Fertigung der Teile. Ohne euch würde die Pumpe funktionieren, noch sähe sie auch nur halb so beeindruckend aus.
Ich danke der ganzen Arbeitsgruppe für die freundliche Kameradschaft.
Auf die Gefahr hin jemanden von meinen Freunden zu vergessen, danke ich euch lieber zusammen. Seien es die Freunde vom Tanzen, aus dem Studium, der Fachschaft, sonstige aus Münster oder meine ältesten Freunde aus Wessum und Umgebung und allen im Rest der Welt. Ohne euch wäre die Zeit des Studiums bestimmt nicht so toll gewesen wie sie es war. Auch habt ihr mich in stressigen Phasen mehr unterstützt als ich euch danken kann.
Ich danke auch Kerstian Schukay für die Tipps zur Verbesserung meines Englisch in dieser Arbeit.

Last but not least danke ich meinen Eltern, Helmut und Gudula für die stets liebevolle Unterstützung. Ohne euch wäre es mir weder möglich gewesen zu studieren, noch es in schwierigen Zeiten durchzustehen. Das gilt auch für meinen Bruder Thomas, der stets durch seine heitere Art mich von anderen Gedanken ablenken kann.